

Maars, tuff rings, and tuff cones at the Manyara rift escarpment, Tanzania.

A Delcamp¹, H.B. Mattsson², L. Gurioli³, E. Sakoma⁴, L. Steyaert¹, M. Kervyn¹.

1. Vrije Universiteit Brussel
2. Uppsala University
3. Université Clermont Auvergne
4. Dodoma University

Audray Delcamp: delcampa@tcd.ie

Hannes B. Mattsson: hannes.mattsson@geo.uu.se

Lucia Gurioli: lucia.gurioli@uca.fr

Engelbert Sakoma : engelbertsakoma@yahoo.com

Lore Steyaert: Lore.steyaert@gmail.com

Matthieu Kervyn: Matthieu.Kervyn.De.Meerendre@vub.be

This paper is a non-peer reviewed preprint submitted to EarthArXiv.

Abstract

About 350 maar craters, tuff rings, and tuff cones are spread along the Manyara rift escarpment, and clustered around the Hanang and Kwahara volcanoes in North Tanzania. They lie in the East African Rift, an active extensional setting, where the magma composition is moderately to highly alkaline and carbonate-rich. We present newly-collected depositional characteristic observations, grain size distributions, and texture analyses of tephra deposits from selected maars, tuff rings and tuff cones of alkaline composition in Manyara to illustrate the range of the associated eruption dynamics and eruptive styles. We observed deposits with some evidence for water-magma interaction and deposits without. We attribute this range to varying magma ascent conditions and water availability along intrusive paths. Magma is guided by fractures allowing it to rise fast and to exsolve gas only near the surface. If water was available within a fracture, a moderate phreatomagmatic eruption was triggered and formed a shallow maar. In a dry fracture, the magma was fragmented by gas exsolution near the surface resulting in a tuff ring or a tuff cone. Several tephra deposits show similarities with kimberlite deposits, notably so the spherical and ellipsoidal shape of the juvenile lapilli and the presence of cannonball bombs.

Keywords: phreatomagmatism, dry fragmentation, alkaline magmatism, East African Rift, Tanzania.

1. INTRODUCTION

Maar volcanoes, tuff rings, and tuff cones, are small volcanic landforms that result from one to several eruptions of small volume (e.g. Bradshaw and Smith, 1994; Freda et al., 2006, Harvey et al., 2009). We refer to these landforms by the common term “monogenetic volcanoes” (de Silva and Lindsay, 2015), although “small volcanoes” has also been proposed to indicate that they can result from several eruptions but will remain of small size (White and Ross, 2011).

Maars are volcanic depressions that cut into the pre-eruptive surface and are surrounded by an ejecta rim, of generally small volume (<10km³) (Lorenz, 1986). The morphology of tuff rings is similar to maar volcanoes but their broad and shallow craters do not cut into the ground (Head et al., 1981; Lorenz, 2003). Tuff cones, as indicated by the name, have a conical shape and form a more pronounced positive relief (Head et al., 1981; Wohletz and Sheridan, 1983). These monogenetic volcanoes have been classically interpreted to result from the interaction between magma and water. Referred to as phreatomagmatism, that interaction involves “wet” fragmentation (Zimanowski et al., 1997; Büttner and Zimanowski, 1998). The amount of water would be the main factor to guide the type of eruption and the resulting edifice morphology (Wohletz and Sheridan, 1983; Sohn, 1996; White, 1996; Vespermann, and Schminke, 2000). Thereby, tuff cones are considered to form when water is abundant (high water:magma ratio), while maars and tuff-rings would form when the water:magma ratio is lower. For maar and tuff ring volcanoes, the classical “Lorenz” model proposes that rising magma meets groundwater and creates violent explosions (Lorenz, 1973). Since the 70’s/80’s, this model has been constantly refined, improved, and broadened with direct observations, analogue experiments, and field observations (eg. Kienle et al., 1980; Riedel et al., 2013; Graettinger et al., 2014; Valentine et al., 2015).

The maars and tuff-rings are composed at depth of feeder dyke(s), sill(s) and a diatreme and their deposits result from complex processes that do not necessarily reflect the deeper diatreme processes (e.g. Levebvre et al., 2013). Diatremes are generally absent below tuff cones. In general, deposits resulting from phreatomagmatism feature dense, blocky juvenile pyroclasts, ash-coated particles, accretionary lapilli, impact sags below large bombs due to plastic deformation of wet layers upon impact and are rich in fine ash.

Other studies suggest that for magmas with ultramafic and alkaline compositions, such as melilitites or carbonatites, there is no need of external water to form maar to tuff cone volcanoes and gas exsolution would drive fragmentation (e.g., Lloyd et al., 1991; Stoppa, 1996; Sparks et al., 2006; Scott-Smith, 2008; Stoppa et al., 2013; Berghuijs and Mattsson, 2013). This process may be restricted to mafic alkaline magmas as they exhibit extreme volatile solubilities and can have very high pre-eruptive volatile contents. For example, an experimental petrology study indicates that melilitic magmas can contain up to 18 wt. % dissolved CO₂ under upper mantle temperature and

pressure (Brooker et al., 2001). Other evidence of volatile-rich conditions is found in the abundance of phlogopite crystals that can hold up to 4 to 4.5 wt. % water in mafic alkaline magmas (Deer et al., 1962). Arguments supporting this hypothesis are based on petrography and mineral geochemistry, although the pre-eruptive volatile contents of the relevant magmas have not yet been quantified in-situ. These deposits also lack typical evidence of phreatomagmatism at the macro- and microscopic scales. As noted by White and Valentine (2016), however, phreatomagmatism produces a wide range of eruptive products with various morphologies and vesicularities, and the absence of typical phreatomagmatic indicators in a deposit is not sufficient to rule out wet fragmentation.

In this study, we present newly-collected deposit descriptions, grain size and texture analyses on six selected maar, tuff ring and tuff cone deposits from two large monogenetic fields (Katesh and Babati) of alkaline composition in Tanzania, along the East African Rift, to investigate the eruptive dynamics. We further aim to ascertain the eruptive processes at the origin of alkaline maar and tuff ring formation: dry or wet fragmentation? These findings can help in the interpretation of other alkaline monogenetic fields along the East African Rift, or elsewhere on Earth, such as the Eifel Volcanic Field (Germany) or the Chaîne des Puys (France).

2. GEOLOGICAL CONTEXT

The East African Rift splits the African continent into two major plates (Fig. 1). This tectonic structure starts in the Afar depression in the north, runs through Ethiopia and splits in two branches, the Western and Eastern branches, south of Lake Turkana in North Kenya (e.g. Ebinger et al., 1997; Chorowicz, 2005; Delvaux and Barth, 2010). The Western branch forms a succession of basins and lakes. The Eastern branch splits from Natron rift, at the boundary between Kenya and Tanzania, into three segments forming the North Tanzanian Divergence Zone. The three segments are, from west to east, the Eyasi, the Manyara-Dodoma, and the Pangani rifts (Macheyeki et al., 2008).

We here focus on the monogenetic fields mostly composed of maars and tuff rings in the Manyara rift, which is part of the Manyara-Dodoma segment (Figs. 1, 2). In the Manyara rift, three monogenetic volcanic fields with a total of ca. 350 craters are situated in both the footwall and the hanging wall of the rift: Basotu, Katesh and Babati volcanic fields (Delcamp et al., 2019). The vents of the latter two are distributed around two nephelinite and carbonatite strato-volcanoes, Kwahara and Hanang (Dawson, 2008; Baudouin et al., 2016). These volcanoes were active during the Pleistocene between 1.5 +/- 1.0 and 0.7 +/- 0.0 Ma for Kwaraha and between 1.5 +/- 0.3 and 0.9 +/- 0.2 Ma for Hanang (K-Ar ages by Bagdasaryan et al., 1973). No age determinations exist for the Manyara monogenetic vents but it is possible that their activity and perhaps plumbing systems were connected to the Kwahara and Hanang volcanoes. All the observed monogenetic vent deposits are

proximal, and no distal deposits have been found. The spatial distribution of the craters within the Tanzanian monogenetic volcanic fields are controlled by the old basement and the rift structures although this influence is fading in recent geological times as the rift is becoming more mature (Delcamp et al., 2019).

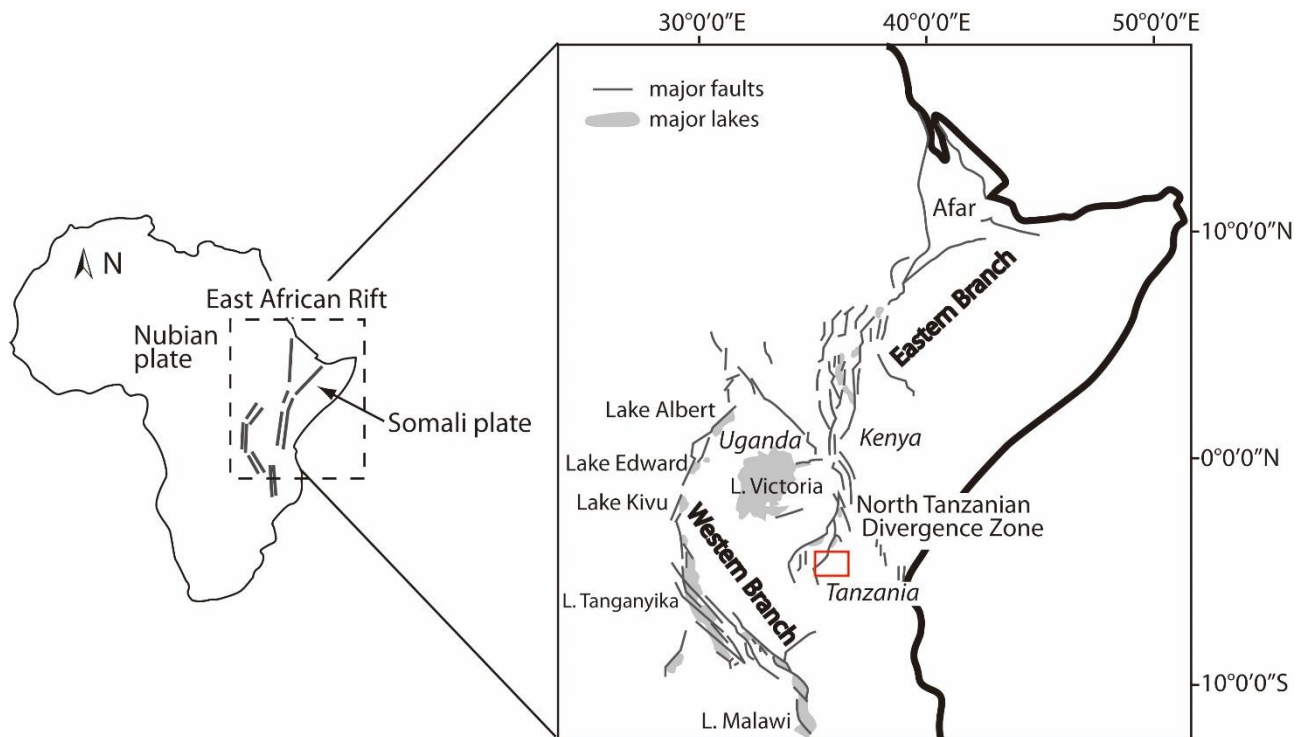


Figure 1: General geological and tectonic context of the East African Rift and the North Tanzanian Divergence Zone (modified from Delcamp et al., 2019). The studied area is marked by a red rectangle.

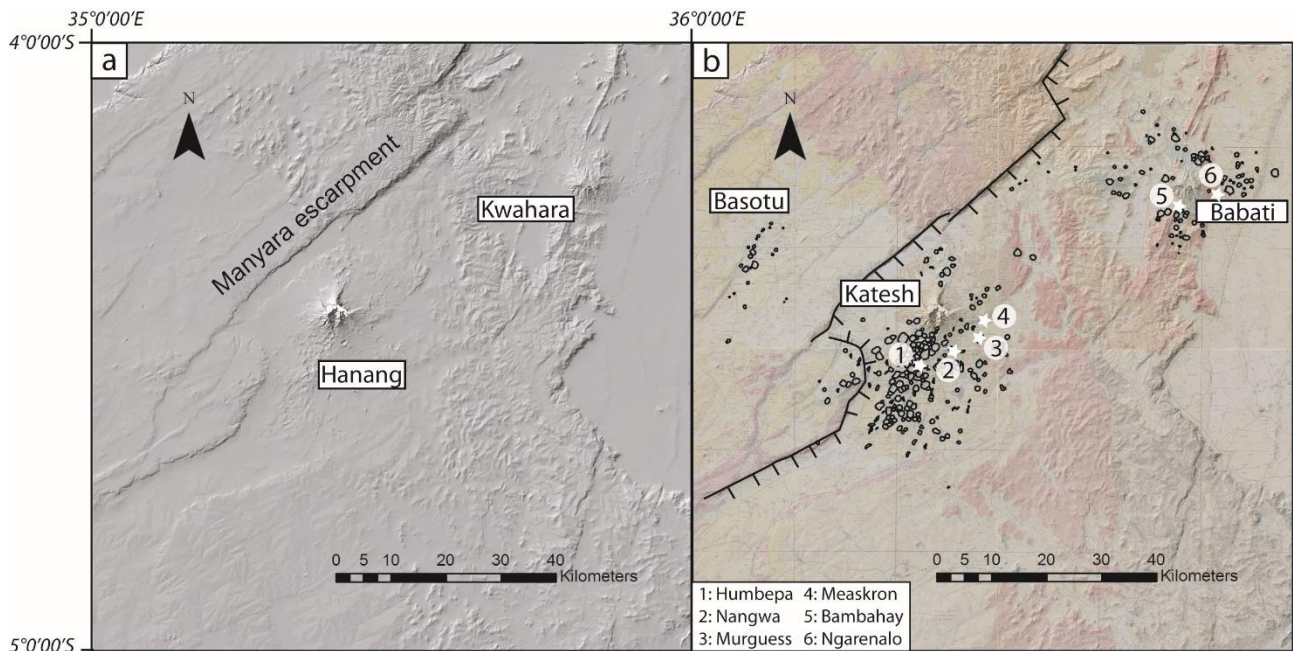


Figure 2: **a.** Shaded relief image derived from SRTM-DEM (30m; [Jarvis et al., 2008](#)) with the Manyara rift escarpment and the strato-volcanoes of Hanang and Kwahara indicated. **b.** Shaded relief image overlapped with the geological map ([Mudd and Orridge, 1966](#); [Thomas, 1966](#)). The monogenetic volcanoes form three fields named after the villages and cities of Basotu, Katesh, and Babati. The craters and the few cones are delineated with black contours ([Delcamp et al., 2019](#)). The studied deposits are marked with a white star.

3. SITE SELECTION AND METHODOLOGY

Six monogenetic volcanoes were selected for detailed stratigraphic studies, grain size and texture analyses of proximal deposits after a survey in the volcanic fields ([Fig. 2b](#); [Table 1](#) for GPS location). These data are complemented with major element analysis ([Table 2](#)). The selection was based on outcrop availability and quality, and we further choose volcanoes that represent the range of morphologies and deposit characteristics observed during our survey. Detailed field pictures with further drawings and descriptions are provided in appendixes. Abbreviations used in the log are listed in the appendix.

Table 1: GPS coordinates of the volcanoes (WGS 84/ UTM zone 36S)

Volcano	GPS Coordinates
Humbepa	S0431480 / E03522288
Murguess	S0429065 / E03528099
Measkron	S0427391 / E03529088
Nangwa	S0430341 / E03525403
Ngarenato	S0414503 / E03551566
Bambahay	S0416080 / E03547129

Table 2: Composition in wt. % oxides of few collected specimens (XRF analyses). HAN: sample from Hanang volcano (lava flow); HUM: sample from Humpeba volcano (pyroclasts); HAN LF: lava flow below Humbepa maar; MEA: sample from Measkron (bomb); MURG: sample from Murguess (pyroclasts); NGA fault: rock-filling fault at Ngarenalo; NGA ball: loaded bomb sampled at Ngarenalo.

	HAN 27 08-1	HAN 27 08-2	HUM4 21 08-A	HUM 7 21 08	HAN LF	MEA 24 08-B	MURG 25 08 H	MURG 25 08 U	NGA fault	NGA ball	SIN 30 08-E
SiO₂	44,537	46,001	42,012	43,672	39,659	42,583	46,793	45,015	14,762	47,353	42,753
TiO₂	1,076	1,537	2,645	2,613	2,614	4,131	2,625	2,751	0,596	2,22	4,123
Al₂O₃	14,529	13,506	9,031	8,852	9,074	7,13	7,662	8,005	2,759	7,83	8,588
Fe₂O₃	7,941	9,951	12,41	12,703	12,202	13,5	10,814	11,646	3,211	11,244	17,78
MnO	0,26	0,276	0,214	0,181	0,214	0,182	0,144	0,156	0,048	0,163	0,277
MgO	1,513	2,006	9,76	9,349	9,55	11,05	15,638	15,802	4,37	12,15	7,069
CaO	9,999	10,054	13,789	10,45	13,309	11,97	7,111	8,213	41,277	11,052	5,958
Na₂O	7,415	6,275	2,612	0,837	3,871	1,481	1,75	1,498	0,4	3,262	4,641
K₂O	3,682	3,484	1,538	1,522	2,484	2,13	2,593	2,026	0,671	1,582	2,687
P₂O₅	0,514	0,6	0,778	0,763	0,632	0,691	0,396	0,427	0,071	0,424	0,887

3.1. Grain size, componentry, and density analyses

We follow the grain size classification of [Berghuijs and Mattsson \(2013\)](#) which distinguishes particle sizes as follow: 1mm fin ash; 1-2 mm coarse ash; 2-30 mm fine lapilli; 30-64mm coarse lapill; >64 mm blocks and bombs. A grain size distribution study was performed at three sites. The sites were chosen based on outcrop sizes to obtain an as complete as possible eruptive sequence from bottom to top in one locality. We sampled almost every visibly different layer at Humbepa, Murguess, and Measkron to presumably represent different eruptive conditions. A problem encountered at Humbepa and Measkron is that deposits are not friable due to cementation or welding. Nevertheless, we sieved most of the units to get an overall idea on the grain size distribution to compare the evolution within a site and between sites.

The samples were dry-sieved from -2.5ϕ to 5ϕ with a 0.5ϕ interval. The sieving was carried out manually for about 2 minutes to avoid any breakage of the clasts. Each size fraction was then weighed with an electronic balance with a precision of 10^{-1} gram, to calculate the weight percent of each size fraction and to calculate the statistic and sedimentary parameters. Here, we determined the statistics (mean, sorting, skweness, and kurtosis) using the Folk and Ward method in the GradiStat spreadsheet ([Blott and Pye, 2001](#)).

Componentry was only determined for few selected samples of representative facies and was performed for the fraction from -3ϕ downward, following the method of [Eychehe and Le Pennec \(2012\)](#). For Humbepa, it was not possible to perform each analysis down to 3ϕ , because of ash coating or particle aggregation. For fractions larger than 0.5ϕ , a binocular was used.

Because of cementation, we expect the original grain size distribution to be shifted towards smaller grain sizes. Note that free crystals were sometimes surrounded by a sub-mm thin coating of ash and are considered as free crystals in componentry. However, cored ash and lapilli have a thicker rim and are considered as juvenile; note that it is only possible to distinguish between cored and loaded clasts when they are broken, and their interiors exposed. Nevertheless, they are both juvenile.

Whole rock density measurements of clasts of $\phi = -2.5$, $\phi = -3$ and $\phi < -4$ were performed using the GeoPyc 1360 pycnometers on selected clasts of mainly Murguess and Measkron deposits. The clasts were previously heated at 70°C for 24 hrs to remove excess water before being weighted and measured for their density. We further tested for micro-porosity with density measurements performed with an He-pycnometer.

Chemical analyses of major and trace elements were done but we only present in this paper major element concentrations. The rock specimens were crushed into a fine powder then fused to produce

glass pills which were then analysed by X-Ray Fluorescence (XRF) at ETH Zürich for major element concentrations.

4. TYPE OF PARTICULES

Based on morphological and textural characteristics performed at different scales (naked eyes, binocular, microscope, Scanning Electron Microscope), five classes of particles were distinguished:

1) juveniles with the following features:

-Rounded and angular ash and lapilli (rounded and ellipsoidal juvenile particles being particularly abundant).

-Most of the larger lapilli clasts displays a “loaded” texture similar to the one reported by Rosseel et al. (2006) for some bombs of the 1886 Rotomahana eruption, where abundant small fragments are dispersed through the bombs. Here, the “loaded” particles are at maximum in the coarse lapilli-size to small bomb-size. They consist of a microlitic groundmass with crystals of phlogopite, olivine, feldspar, and sometimes lithics that are distributed in a circular pattern (Fig. 3). “Cored” lapilli are made of a large crystal at the centre (typically a phlogopite) surrounded by a microcrystalline groundmass. Rounded (cored or loaded) lapilli can be embedded in a larger loaded lapillus. The cored and loaded bombs are often rounded with a cannon-ball shape. Vesicles are rarely observed. These textures are also found in the coarse-ash fraction.

2) Felsic lithics: plutonic (mainly granite) and metamorphic basement clasts, 3) melilitic lava flow clast in the Humbepa maar deposit: angular, black, shiny, microcrystalline particles, 4) free crystals: mainly feldspar, pyroxene, and phlogopite, 5) aggregates of particles due to cementation.

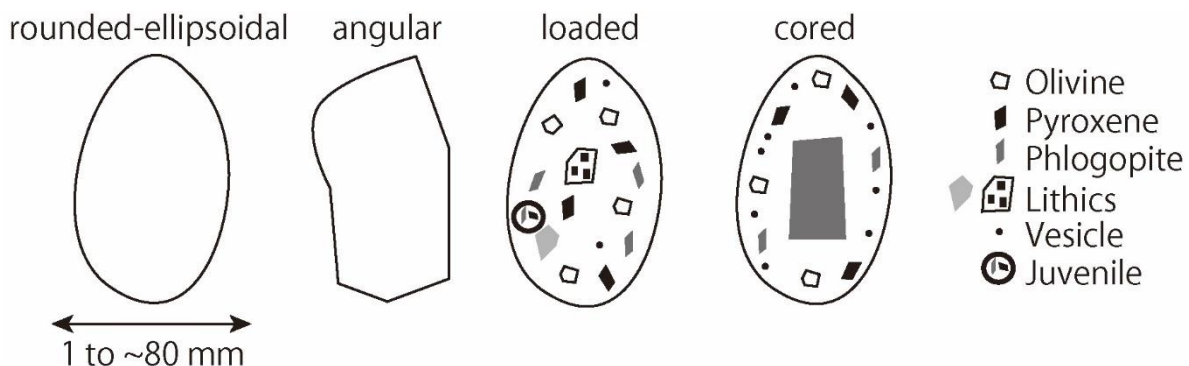


Figure 3: Simplified sketch of the different types of juvenile textures observed at the macro and microscale (coarse ash to small bombs). Most of the juveniles are spherical to ellipsoidal, but few are angular. Loaded juveniles consist of phenocrysts and sometimes lithic and/or smaller juveniles dispersed in a microlitic to glassy groundmass, while cored juveniles consist of a large crystal (typically phlogopite) surrounded by a thin rim of a microlitic to glassy groundmass.

5. FIELD DESCRIPTION

5.1. Humbepa (HUM)

Humbepa is a shallow nephelinite maar ([Table 2](#)) with a ~800 m diameter crater with a flat crater floor surrounded by a circular tephra ring opened to the north north-east. Available outcrops (proximal deposits) stem from quarrying ([Fig. 4a](#)). The crater floor is at about 10 to 15 m below the surrounding topography and the crater cuts into a massive melilite lava flow (HAN-LF; [Table 2](#)). The lava flow has microlitic texture with crystals of green clinopyroxenes, nephelines, and oxides. Our log section is oriented N-S and the outcropping beds are overall N140-10E. The outcrops for Humbepa are referred as follows: the three first letters correspond to the name of the volcano, the number corresponds to the outcrop number, and the letter to the unit. For example, HUM3A corresponds to Humbepa, outcrop number 3, unit A.

A facies is defined by a unique character that distinguishes it from other facies ([Cas and Wright, 1987](#)). The character may be compositional, textural, or may be based on sedimentary structures. In Humbepa, we distinguish three facies based on sedimentary structures and bedding-types: massive ash beds and laminae (facies α ; [Fig. 4b](#)), mm-thin laminae sometimes diffusely stratified (facies β ; [Fig. 4c](#)), and massive and strongly unsorted cm- to meter-thick breccia beds (facies γ ; [Fig. 4d](#)).

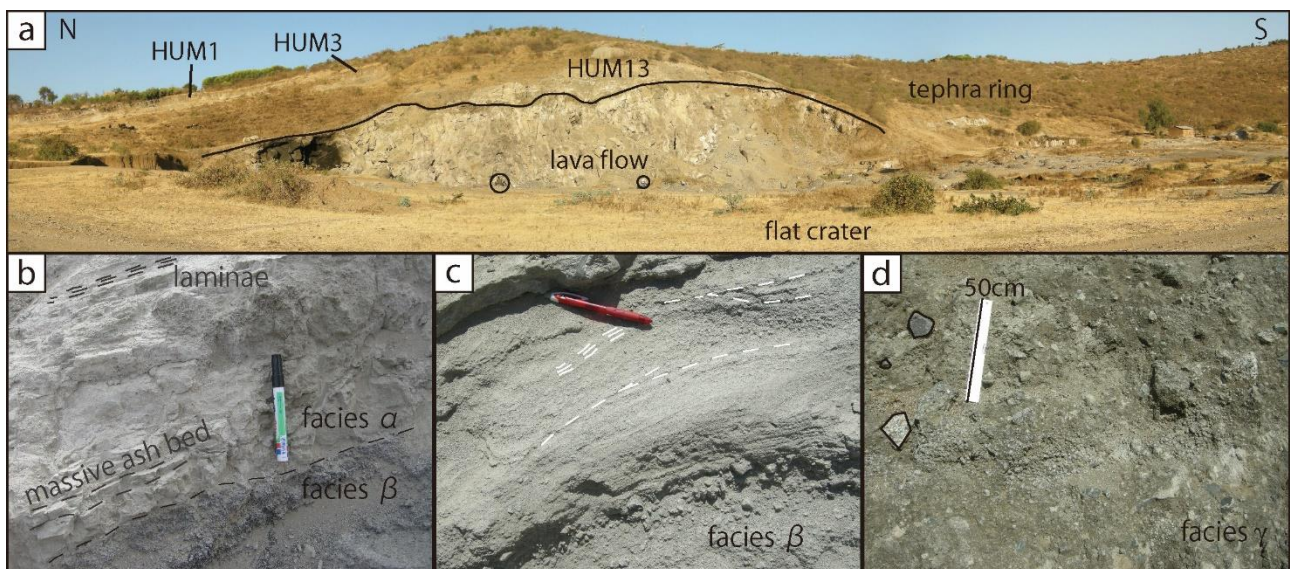


Figure 4: Humbepa maar. **a.** Panoramic view of the quarry showing the lava flow below the maar deposits. Working woman and man encircled for scale. **b.** Facies α consists of massive ash-rich beds or laminae with few lithics (HUM9-22/08-A). Massive ash bed and few laminae are highlighted with dashed brown lines. **c.** Facies β made of mm-thin laminae with discrete cross-bedding (HUM12-E3); few laminae and cross-bedding are highlighted. **d.** Facies γ is a breccia rich in lithics; few lithics are highlighted.

The facies are resumed in **Figure 5** with a partial log of Humbepa; the full log is available in the appendix. There is no specific pattern in facies distribution and no lateral continuity of the facies was observed. The deposits are often indurated with whitish to brownish cement. It is not clear solely from field observations if the induration is due to a primary or a secondary process. We observed this type of induration in few other craters around Hanang and Babati but it is not ubiquitous. The top of the deposit is a soil derived from volcanic material. Humbepa deposits contain angular Precambrian basement (granite and gneiss) and mantle (pyroxenite or hornblendite) xenoliths. We noticed no lateral or vertical spatial distribution pattern of these fragments within the available outcrops. Angular fragments of the melilite lava flow are ubiquitous throughout the deposit, and it is sometimes difficult to distinguish juvenile fragments from these accidental lithics when small although the lava flow fragments tend to have a glassier texture. The granite and gneiss xenoliths are in general fragile and break easily while the other xenoliths are more resistant. Most of the xenoliths are <10 cm across but we noticed few large basement bombs > 50 cm across.

The facies α (**Fig. 6a**) is made of a fine ash matrix embedding angular lithics, crystals belonging to lithics such as microcline and other feldspars (xenocrysts), and free juvenile Ti-clinopyroxene (likely augite), phlogopite, and plagioclase crystals. The thicknesses of individual beds are not constant. The matrix can be sometimes welded or cemented. In thin section, the matrix is tachylitic of brown colour. The lithics and free crystals are oriented forming parallel bedding. The ash and lapilli of facies β (**Fig. 6b**) are mostly spherical, can contain pin-size vesicles, and are sometimes deformed in a ductile manner. The colour of the hand-samples varies from grey to red to yellow. The ash and lapilli are made of clinopyroxenes, few olivines and undetermined needle-shape crystals (yellowish in polarised light and extinguished in cross-polarised light), embedded in a tachylitic dark glass. We interpret the needles to be altered phlogopite crystals. In facies β , the juvenile content can vary from unit to unit but remains higher than the lithic content. Few cm-thin massive ash beds of facies α are sometimes intercalated between coarse-ash and fine-lapilli laminae of facies β (e.g. HUM6-E, HUM12B-E5). The facies β ranges in thickness from 20 cm to about 200 cm.

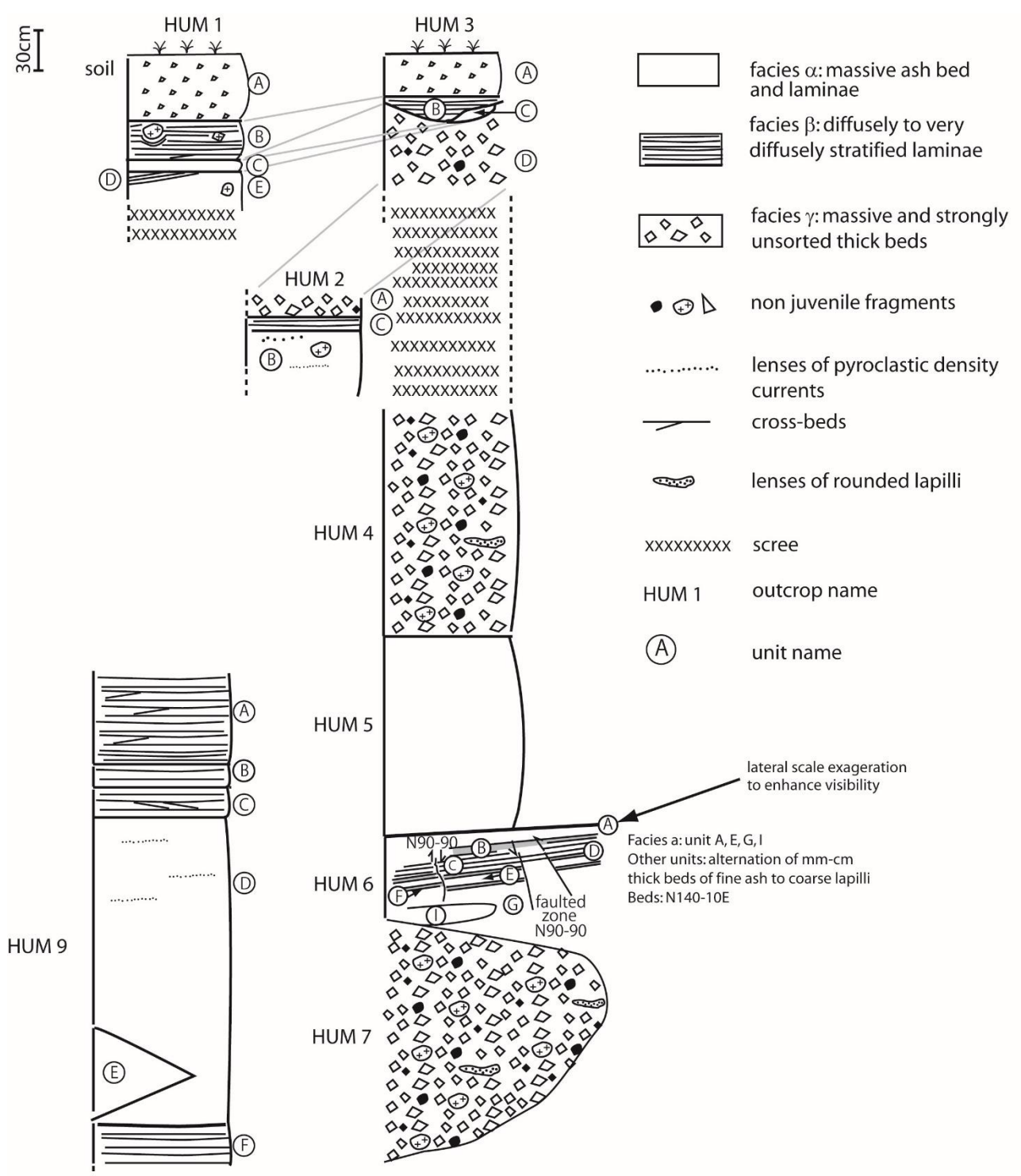


Figure 5: Stratigraphic log of Humbepa.

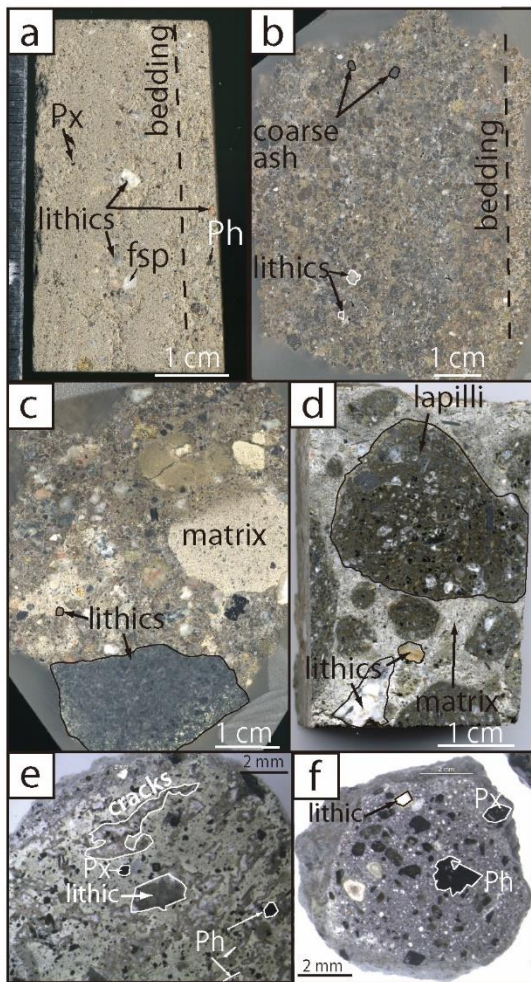


Figure 6: **a.** Facies α : Indurated rock slab of ash-rich laminae with few lithics (HUM12-23/08-E1). Bedding orientation is marked by a dashed line. Px: pyroxene, Ph: phlogopite, fsp: feldspar **b.** Rock slab of facies β with fine and coarse ash, fine lapilli, and lithics organised in a discrete bedding marked by a dashed line (HUM3-B). The juvenile ash and lapilli are mostly rounded or ellipsoidal. **c.** Rock slab of facies γ (breccia) with lithics of various sizes enclosed in a yellowish matrix (HUM7). The colour difference of the matrix is due to epoxy impregnation. **d.** Rock slab of a cluster of juvenile rounded lapilli found in facies γ (HUM4). The lapilli consist of clinopyroxenes, phlogopites, few olivines, few lithics and xenocrystals in a microlitic to tachylyte groundmass, forming loaded lapilli. Note the circular pattern of the microlites and the fluidal and ductile texture of the clast. **e.** Fine lapilli of facies γ at HUM7 where phlogopite and clinopyroxene are within a white glassy groundmass. **f.** Fine loaded lapilli of facies β at HUM9-D2 with oriented crystals and lithics.

The facies γ (**Fig. 6c**) is lithic-rich compared to facies α and β but contains also many juvenile lapilli that are spherical or deformed in a ductile manner (**Fig. 6d**). The lapilli can be found as clusters, lenses, or dispersed within the breccia. Their colour varies from grey to white/yellow (**Figs. 4d and 6d**). Several lapilli display two colours as seen by the naked eye, but this colour difference

vanishes under the microscope, indicating rather superficial alteration than compositional magma mingling. One juvenile lapillus has a very white glassy groundmass (**Fig. 6e**). In thin sections, the juvenile lapilli are composed of green clinopyroxene, phlogopite, and olivine crystals, embedded in a tachylitic, microlithic glass. These crystals can be surrounded by a quenched glass rim as well as the juvenile lapilli itself. Lithic fragments and juvenile rounded lapilli can be found within larger juvenile clasts forming loaded lapilli. The breccia matrix between the juvenile lapilli and the lithics is mostly white to yellow and can be porous. Under polarised light, the matrix is dark to light brown with some carbonate infill, as testified with the typical high birefringent colours.

In summary, the juvenile ash and lapilli in Humbepa are mostly spherical or ellipsoidal and some of them are deformed in a ductile manner (fluidal texture, flattened shape, etc); they consist of a tachylitic groundmass with microlites of (in order of abundance) clinopyroxene, phlogopite, and olivine. They have rare pin-sized vesicles. Trachytic texture and loaded ash and lapilli are common (**Figs. 3 and 6f**). Rare cored ash and lapilli were observed. However, binocular observations of ash revealed lithics and crystals surrounded by a thin fine-ash coating, which occasionally presents cracks.

Two units show beds with subtle sags resembling impact-sag structures; however they are so subdued that an origin from ballistic impact remains doubtful (HUM1-B; HUM12A-D). Low-angle cross-bedding and discrete antidunes were observed in facies β . Accretionary lapilli was only found as isolated clusters and lenses in HUM12A-D.

5.2. Murguess (MURG)

Murguess is a half crescent-shape basanite tuff ring of about 60-m-high open to the south-east. There is only one outcrop available here, but the stratigraphic section (proximal deposit) is almost complete from bottom to top. We hence consider this tuff ring as one single outcrop in our label (MURG). The layers of the outcrop are dipping 30°W (**Figs. 7a, b**). We defined the facies based on grain size and internal stratification (**Table 3**).



Figure 7: Murguess tuff ring. **a.** Murguess deposits, unit A being the lowermost outcropping unit. **b.** Partial stratigraphic log of the section observed in **a.** with the illustration of the difference between the type of stratification (VDS: very discrete bedding; DS: discrete bedding; M: massive unit; L: laminae). Unit A: Juvenile-rich angular and subrounded with abundant rounded lapilli. Unit B: Juvenile rich, angular but mostly subrounded fine and coarse lapilli. Unit C: Lense of lapilli. Unit

D: Laminae of coarse ash but also lenses of fine lapilli. (full and detailed descriptions can be found in the annex). c. Ellipsoidal loaded bomb made of juvenile magma that wraps a basement xenolith, MURG24/08-A. Note the agglutination of magma forming small ellipsoidal melt droplets at the surface d. Spherical, ellipsoidal, and angular ash and lapilli from MURG25/08-U. Most of the juvenile ash and lapilli are subrounded and the larger clasts have cracks on their quenched surface.

Table 3: Facies of Murguess deposits based on grain-size and stratification.

Grain size	Stratification	Unit
Fine ash to coarse ash	Very Discrete Bedding (VDS)	N; J; X
	Discrete Bedding (DS)	B; L
	Laminae (L)	D; F; H; M; N; O; T; Z
	Massive (M)	I; P; R; V; Y
Fine ash to coarse lapilli	VDS	A; E; G; H; U; W
	M	C; K
	DS	Q; S

The deposit is juvenile-rich, with an abundance of sub-spherical to ellipsoidal lapilli and small cannonball bombs, with free crystals of olivine, pyroxene, and large phlogopite that can reach up to 3 cm long (Figs. 7c, d). Xenoliths of granite and lava (basement lava) are found across the tuff ring. Similar to Humbepa, the granite xenoliths are fragile and break between fingers.

We defined several units based on the different facies (Table 3). Unit thickness ranges from about 1 cm to 4 m thick. Occasional internal stratifications are mm to cm bedded. The depositional units and beds are mainly clast-supported, and a few of them inversely graded. Low-angle cross-bedding is observed. Impact sags and accretionary lapilli are absent. The deposit is indurated only at the top of the section.

The shape of the juvenile particles varies from angular to predominantly spherical. All juvenile particles have similar textures: they can be both loaded or cored, similar to those of Humbepa (Fig. 8a, b, c, d). Textures observed on a macroscale are similar to the ones at a microscale. Juvenile particles consist of olivines, phlogopites, and clinopyroxenes, with occasional xenocrysts and xenoliths, enclosed in a glassy (tachylyte) or microlitic light grey groundmass with few pin-size vesicles. The microlites include olivine, nepheline, yellowish needles with low birefringent colours (possibly altered plagioclase?), and oxides. The crystals and lithics are sometimes organised in a circular pattern following the outer shape of the juvenile (trachytic texture) or the large crystal in the case of cored juvenile. Phlogopites can be automorph, xenomorph, with dissolution-like patterns, or deformed Olivines and clinopyroxenes are automorph but some present dissolution

patterns. Fractured pyroxenes are observable on clast slabs. Occasionally, a cored juvenile (ash or lapilli size) can be enclosed within a larger juvenile and vice-versa (**Fig. 8b**). The surface of the juvenile is covered by adhering ash and is sometimes cracked or striated (**Fig. 8e**).

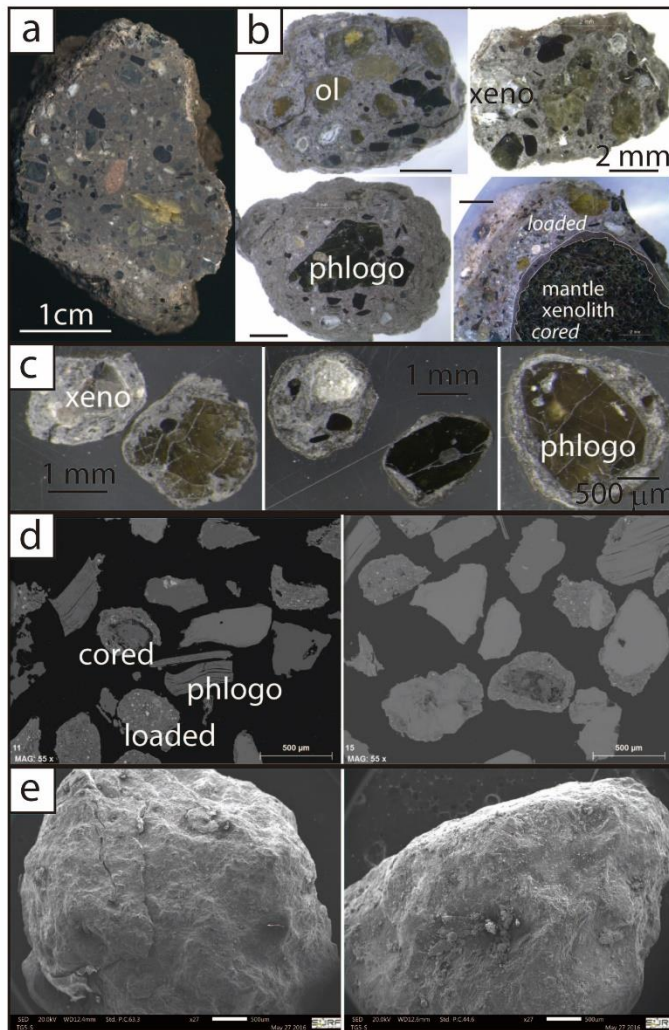


Figure 8: Details of the textures observed in Murguess deposits at various scales. In **a, b, c**: Black crystals: phlogopite (phlogo), clinopyroxene (cpx); green crystals: olivine (ol); white crystals: xenocrystals derived from lithics (xeno). The white and red fragments are lithics. **a.** Angular coarse lapilli with loaded texture. The shape of the juvenile clast is unrelated to their texture and both, angular and rounded clasts, show loaded or cored textures. **b.** The upper pictures are from left to right, angular and ellipsoidal loaded lapilli ($\phi = -2.5$); the bottom pictures show ellipsoidal cored lapilli with (from left to right), trachytic texture around the phlogopite ($\phi = -2.5$) and a cored mantle xenolith loaded in a larger lapillus. The black scale bar indicates 2 mm. **c.** Rounded and angular coarse ash with loaded and cored textures ($\phi = -0.5$). **d.** Back-scattered electron (BSE) microscope images of fine ash showing similar loaded and cored texture ($\phi = 1.5$). Note the deformed phlogopites. **e.** Surface of fine lapilli ($\phi = -2$) as observed under the scanning electron microscope (SEM) with adhering ash, quenching cracks, and stepped fractures.

5.3. Measkron (MEA)

The studied section forms a positive relief, only few meters high, near the Measkron village, hence the name of the section since there is no specific name for this small nephelinite tuff cone. The deposits consist mostly of crudely stratified coarse ash to coarse lapilli that are vesicle-poor and sub-angular (**Figs. 9a, b**). Some of the particles are welded together forming larger irregular clasts, but no fiamme are observed. Crude cross-bedding is observed. Fragmented xenoliths (granite-like and massive peridotite-like), free phlogopite, olivine and pyroxene crystals are found throughout the deposit. Ash and lapilli are mostly angular but several spherical to ellipsoidal clasts were observed (**Fig. 9c**). Some lapilli and bombs are covered by a secondary glassy, opaque, smooth, and green mineral of unknown origin. Only loaded ash, lapilli, and bombs have been observed and cored clasts are absent. Under the microscope, phenocrysts of olivine (iddingsite), clinopyroxene, and phlogopite are embedded in a tachylytic matrix. Some xenocrysts of plagioclase and microcline are surrounded by a rim of a darker tachylyte, potentially caused by disequilibrium with the tachylyte matrix. Some xenocrysts are partially or totally resorbed and have been replaced by secondary minerals as shown by the birefringent colours. Oxides are quite abundant. Fluidal textures with microcrystals surrounding the largest phenocrysts are common. Some large phenocrysts are surrounded by a quenched tachylyte. Micro-vesicles are observed here and there. The surface of lapilli and bombs is occasionally covered by secondary minerals (clays) and/or display protuberances.

Along the section, a lateral facies variation from W to E is observed, where the maximum grain size decreases and several lenses and non-continuous thin beds are observed towards the east. There, the ash and lapilli are more spherical, with more cannonball bombs.

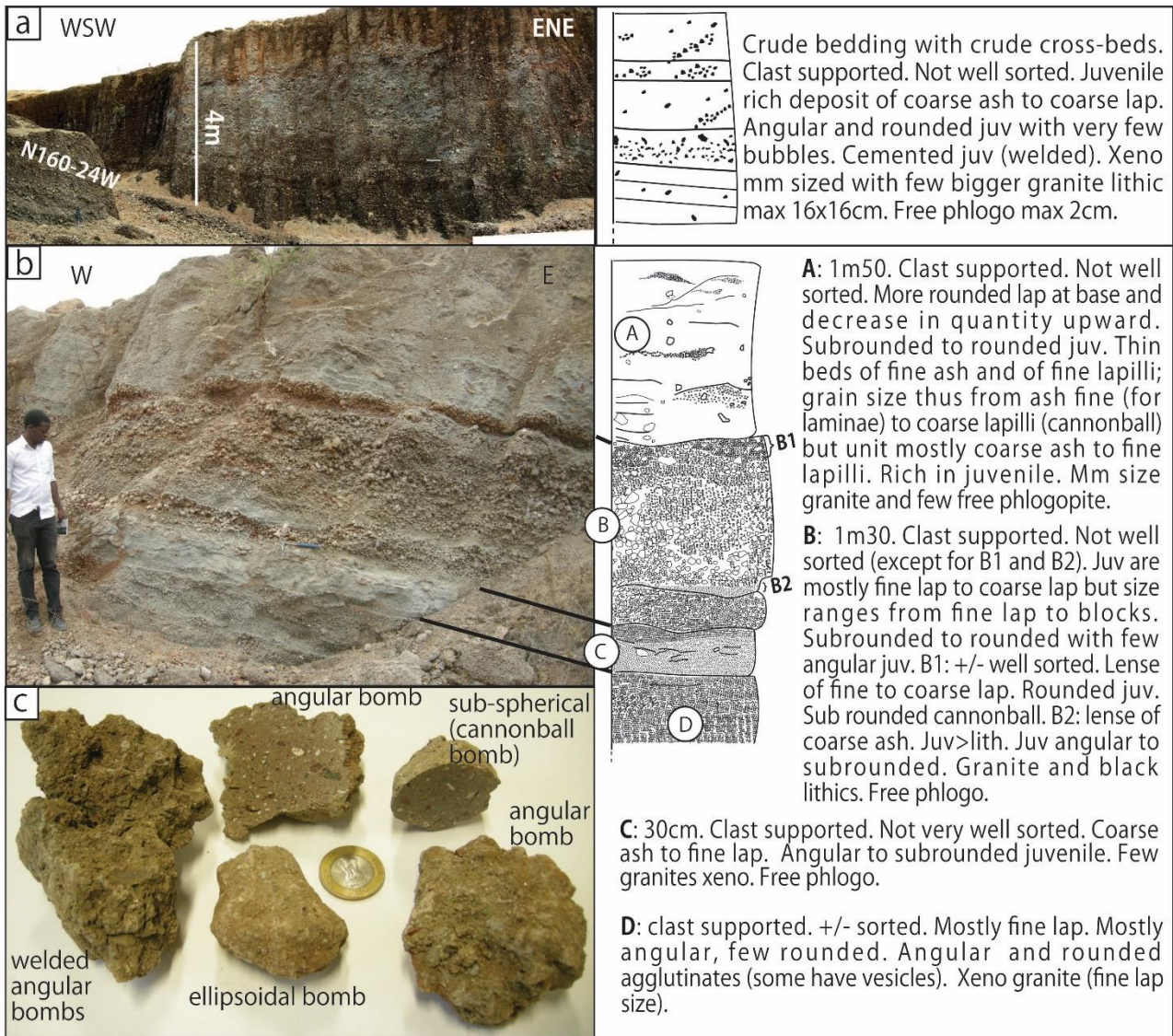


Figure 9: Measkron tuff cone. **a. and b.** Section of Measkron deposits with stratigraphic log. **c.** Few loaded angular and ellipsoidal bombs from MEA3-24/08-B.

5.4. Nangwa (NAN)

A small quarry exposes about 4 meters of the upper section of a tuff ring sequence near Nangwa village. No chemical analysis has been performed but the phenocryst phases are olivine, pyroxene, and phlogopite embedded in a greyish matrix, suggesting a basanitic or nephelinitic composition. The tuff ring forms a crescent shape open to the south-east and its crater is about 50 m deep from its rim. The deposits are cemented by a whitish material, but it is not possible to determine its primary or secondary origin, even using XRD which gave several possibility of clays that are related to a hydrothermal system. Some research should be further done since knowing the origin of clays would give keys to understand the role of fluid in the system.

The two main facies are (α) stratified to diffusely stratified mm-thin laminae and (β) massive beds

(Fig. 10).

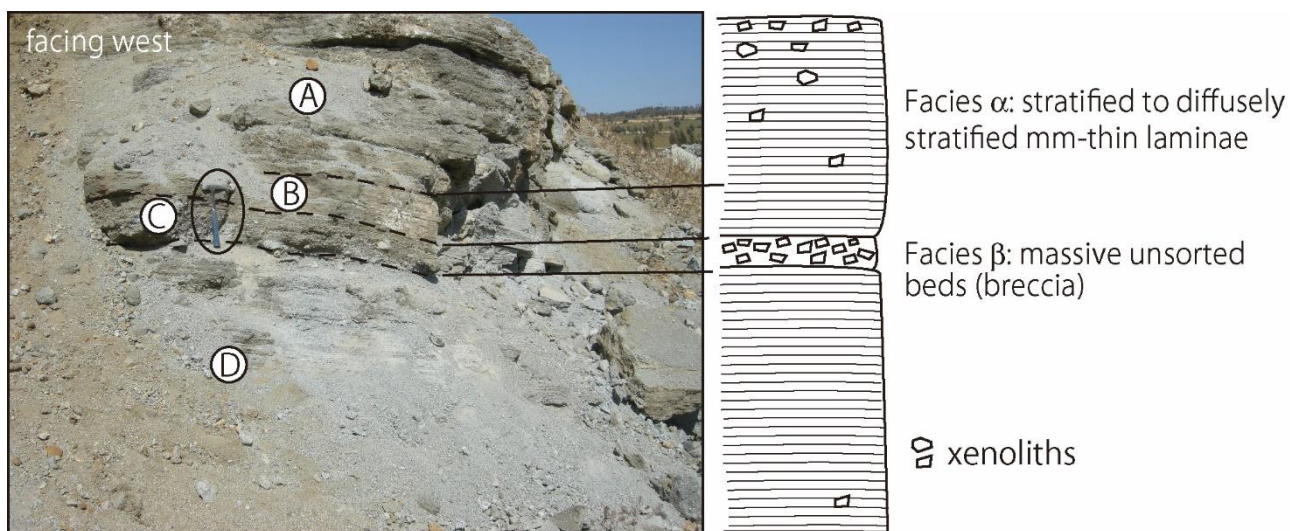


Figure 10: Nangwa tuff ring deposits and its two facies. Units are indicated by a letter within a circle. Hammer in black circle.

In facies α , the particle size distribution changes from one unit to the other but the juveniles are of fine ash to fine lapilli in size (<5 mm). Facies α is dominated by juvenile particles. The juvenile ash and lapilli are mostly angular with only few spherical and ellipsoidal lapilli clasts. Few lithic-rich lenses are found in unit A; in some parts of the quarry, the grain size of the lithics in the lenses increases and reaches up to 5 cm across. Few low-angle cross-bedded layers are observed at the base of units A and F.

Facies β is a matrix-supported breccia composed of fine ash (unit E) or angular coarse ash (unit C) with xenoliths. Few spherical and ellipsoidal lapilli are observed in unit C. A rough grading is observed in unit E, and in certain areas in unit C, with the larger lithics at the top of the unit (inverse grading).

Free mm-sized phlogopites are found across the quarry; they reach 2 cm across in unit E. The xenoliths are angular and stem from the local basement (carbonates, granitoids, and lavas). A vertical or lateral pattern of xenolith distribution was not noticed, and mantle xenoliths were not found.

5.5. Ngarenalo (NGA)

Ngarenalo tuff ring (Sodomango village) forms a discrete nephelinite-basanite crescent-shaped ca. 70 m-high structure opened toward the east (Fig. 11) without an obvious crater. The deposits are used by the locals as a building stone and outcrops are limited to quarries.

Four facies are observed in the exposed deposits: Facies α consists of discrete laminae, facies β of crude beds, facies γ of massive fine ash with few clast-supported lenses, and facies δ of unsorted and clast-supported juvenile material. In all of the facies, sorting is usually poor, with abundant free phlogopite, and the proportion of juvenile particles is greater than that of xenoliths and lithics. The ash and lapilli clasts are angular or rounded.

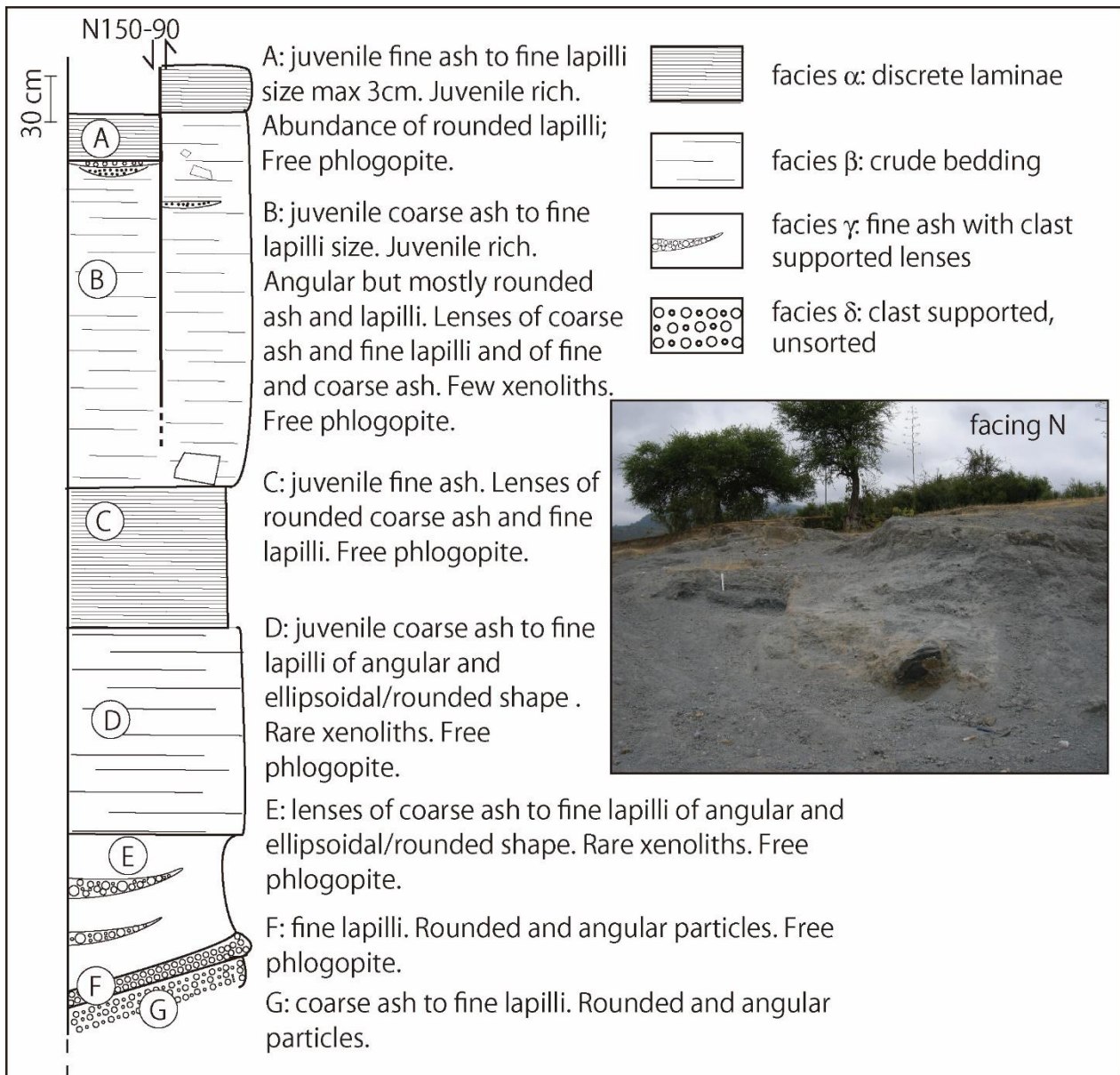


Figure 11: Photo and stratigraphic log of Ngarenalo tuff ring deposits.

The deposits are characterised by the abundance of spherical and ellipsoidal lapilli with sizes up to 5 cm in diameter (Fig. 12a). The lapilli are made of phenocrysts of olivine, clinopyroxene, phlogopite, and plagioclase that are dispersed in a dark-grey matrix. The phlogopites are sometimes deformed or resorbed with a wiggly outline. Rare xenoliths of granite and aphyric lava are found among the lapilli. Occasionally, two colours of matrix are observed: a light and a dark

grey matrix (similar to some juveniles of Humbepa). The two colours of the matrix are visible under polarised light but vanish under crossed-polarised light. A discrete microvesicularity exists with pin-size rounded and sheared bubbles. The microcrystals dispersed in the matrix are mostly olivine, pyroxene, phlogopite, plagioclase, and oxides. Trachytic texture can occur in some spherical and ellipsoidal lapilli. Smaller sub-spherical ash and lapilli are sometimes embedded within a larger spherical or ellipsoidal lapillus forming loaded lapilli. Observations of lapilli slabs under the binocular revealed resorbed phlogopites with an irregular but smooth and rounded contour, white microlites of feldspar, and occasional clasts of rounded juveniles encompassed in a larger loaded juvenile. Green amphiboles were observed in some juvenile clasts.

The deposit is cut by a set of conjugate fractures \sim N80 and \sim N130 that are sometimes filled with a yellowish to whitish breccia consisting of carbonatite and rounded juveniles, fine lapilli in size, and free crystals of olivine and plagioclase (**Fig. 12b**).

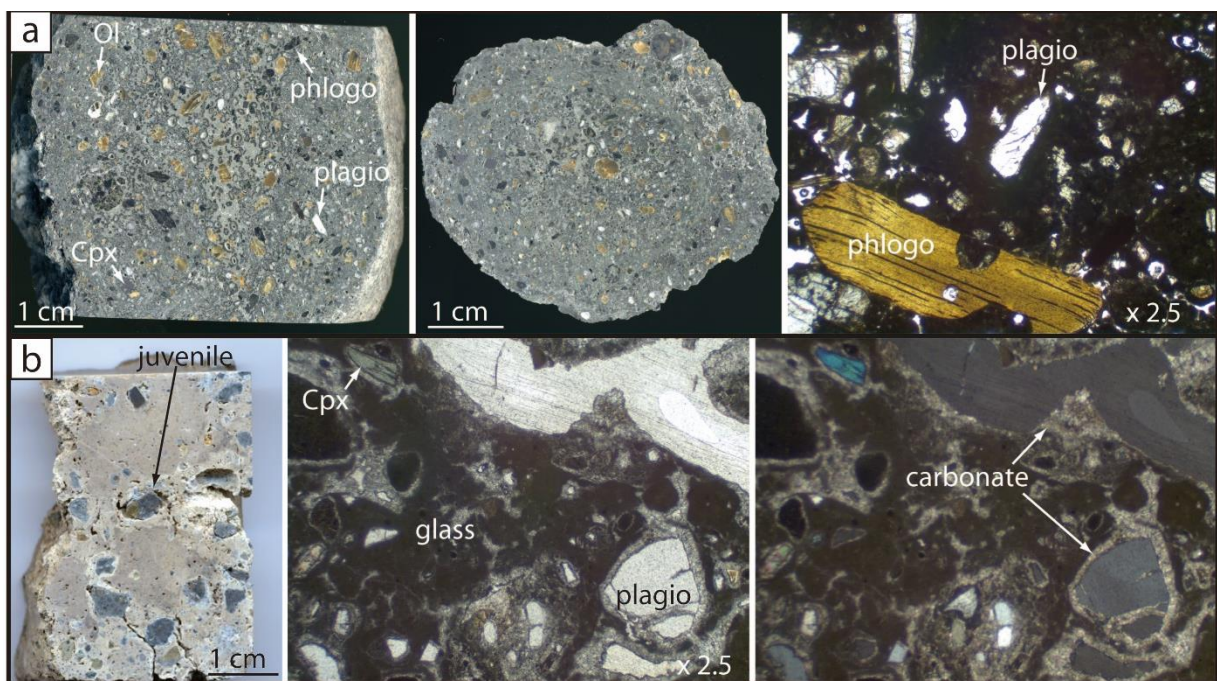


Figure 12: a. From left to right: Ellipsoidal lapilli slabs and one frame of the corresponding thin section. On the left photo, two colours of matrix (a light and a dark grey) are distinguishable. The middle photo shows a trachytic texture. The lapilli consists of phlogopites, olivines, clinopyroxenes, plagioclases and few lithics dispersed in a tachylitic matrix as seen in the thin section under polarised light. **b.** From left to right: Secondary carbonates filling the faults in Ngarenalo. The breccia is made of sub-ellipsoidal juvenile and free crystals embedded in a carbonate matrix. Breccia observed under plane polarised light (middle) and cross-polarised light (right).

5.6. Bambahay (SIN)

This outcrop is located between several craters. Because no unconformities are observed, we assume that the provenance of the units is the same vent for the whole outcrop. The layers dip towards the east and we deduce that the corresponding crater may be the one directly west of the outcrop (**Fig. 2b**).

Several facies are observed as shown in Figure 13. Spherical and ellipsoidal ash and lapilli are still found but the deposit is dominated by angular particles. Erosional channels and few antidunes are observed between units B and C. A black clast-supported subaphyric scoria layer of basanite composition (unit E) has an undulating contact with unit F. Accretionary lapilli (with their distinctive ash coating layers) are observed in the massive ash units H and J. Fine yellow ash layers form wavy beds at the base of unit I; these fine yellow ash layers are also intruded by grey material of unit I. Except for unit E, the petrographic composition of the juvenile ash and lapilli is a blend of pyroxenes, olivines, and phlogopites.

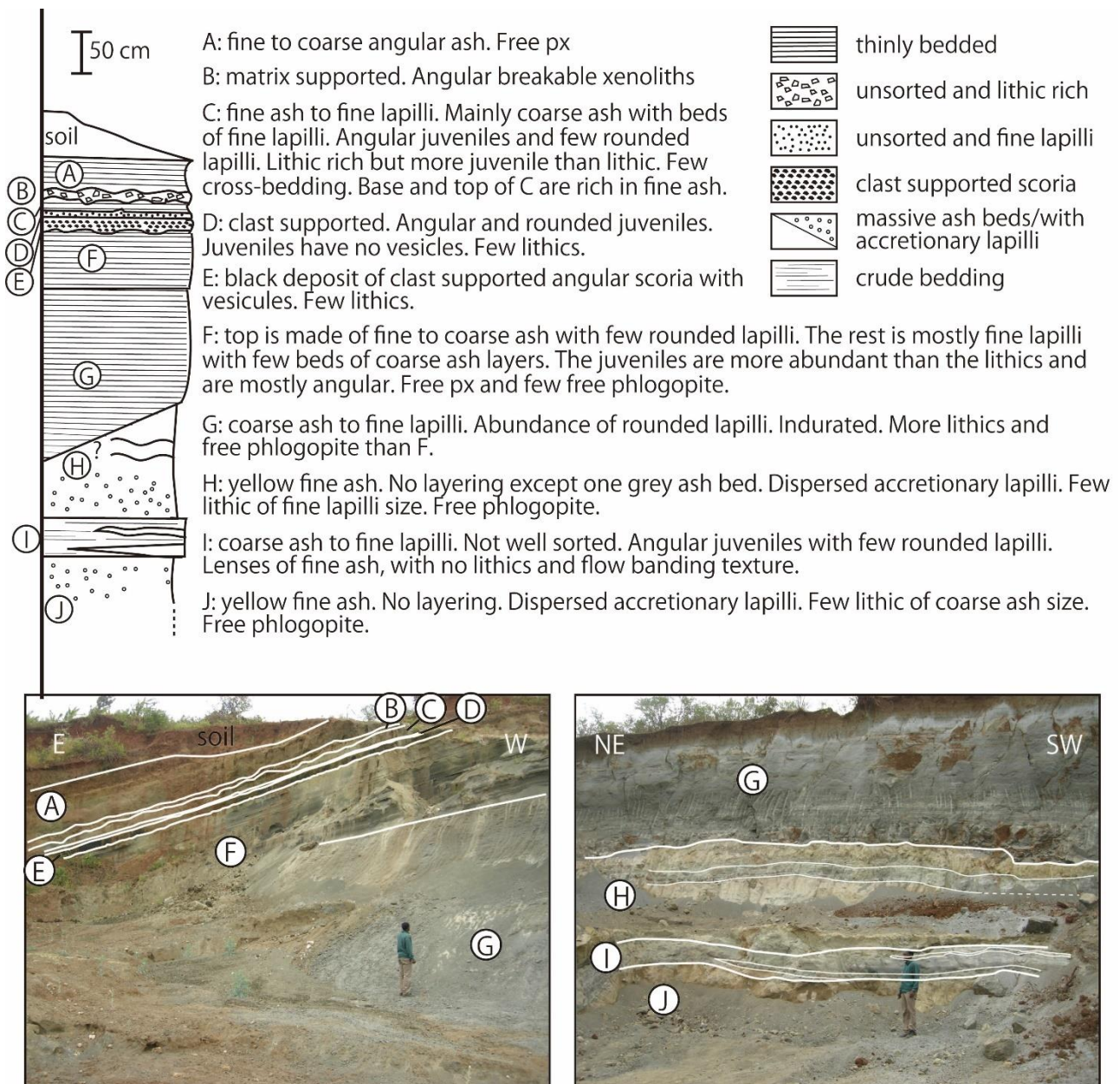


Figure 13: Picture and stratigraphic log of Bambahay.

6. GRAIN SIZE DISTRIBUTION, COMPONENTRY, AND DENSITY.

6.1 Humbepa (HUM)

For Humbepa, the grain size distribution is either uni- or bimodal (**Fig 14a; table 4**). One sample (HUM1-21/0/-A) corresponding to the soil, is trimodal, reflecting soil formation (disaggregation, aggregation).

For facies α , sieving results generally correspond with field observations. The facies α is mainly well-sorted (**Cas and Wright, 1987**) although bimodal. The bimodal shape is due to the larger accidental lithics that occur towards the larger grain size.

For facies β , the results might be biased due to particle clustering. Nevertheless, most of the trends are unimodal and well sorted within a bed, but the mean grain size varies across beds.

For the facies γ , most of the layers are poorly sorted with larger mean grain size.

Skewness varies across the deposit. Although care in the interpretation of these data is needed due to the possible influence of particle clustering, the results are generally in good agreement with the qualitative observations at the outcrop scale.

The componentry analyses confirm the field observations where Humbepa units are rich in lithics, but lithic content remains however smaller than that of the juveniles.

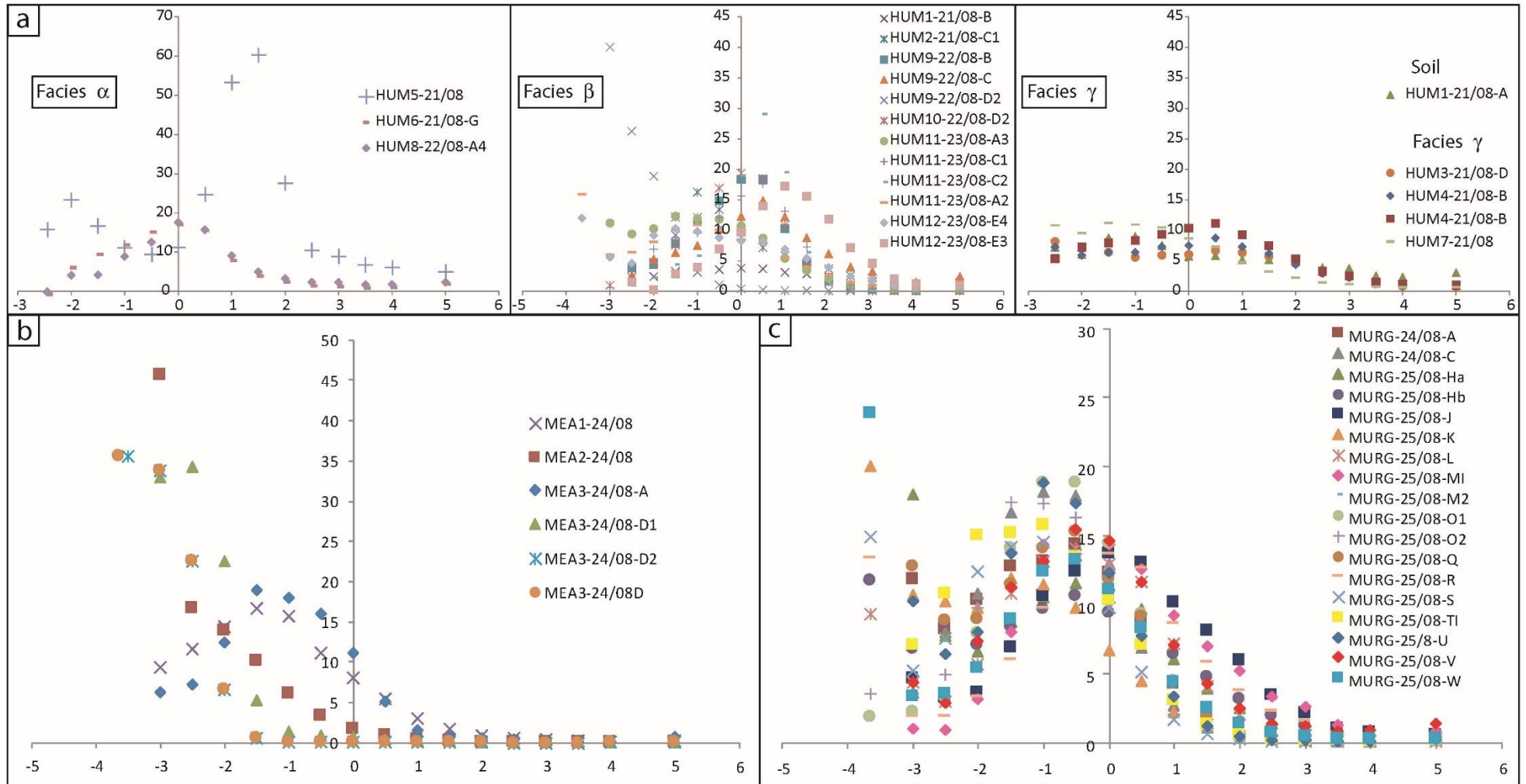


Figure 14: Grain-size analyses for **a.** Humbepa, **b.** Measkron and **c.** Murguess deposits. Grain -size distribution and statistics, along with componentry and density analyses are available in the annex.

Table 4: Results of grain-size analyses; note that the quality of the sorting in the table corresponds to the Folk and Ward scale, which is different from the one used in volcanology where the quality of the sorting is always poorer than sedimentary deposit.

Tri: Trimodal, Bi: Bimodal, Uni: Unimodal. VPS : very poorly sorted, PS : poorly sorted, MS: Moderately Sorted, MWS: Moderately Well Sorted. Platy: platykurtic, Meso: mesokurtic, Lepto: leptokurtic.

HUMBEP A		HUM1-21/08-A	HUM1-21/08-B	HUM2-21/08-B	HUM2-21/08-C1	HUM3-21/08-D	HUM4-21/08-B (1)	HUM4-21/08-B (2)	HUM5-21/08	HUM6-21/08-G	HUM7-21/08	HUM8-22/08-A4	HUM9-22/08-B	HUM9-22/08-C	HUM9-22/08-D2	HUM10-22/08-D2	HUM11-23/08-A2	HUM11-23/08-A3	HUM11-23/08-C1	HUM11-23/08-C2	HUM12-23/08-E3	HUM12-23/08-E4	
SIEVING ERROR:		0.1%	0.2%	0.4%	0.4%	0.8%	0.1%	0.7%	0.9%	1.7%	1.1%	1.3%	0.4%	0.4%	0.0%	0.1%	0.2%	0.0%	0.1%	0.2%	0.2%	0.1%	
SAMPLE TYPE:		Tri, VPS	Uni, PS	Bi, VPS	Bi, PS	Bi, VPS	Bi, VPS	B, PS	Bi, PS	Uni, PS	Bi, PS	Bi, PS	Uni, PS	Uni, PS	Uni, MWS	Uni, PS	Bi, PS	Uni, PS	Uni, PS	Uni, PS	Uni, MS	Uni, PS	Bi, PS
TEXTURAL GROUP:		Sandy Gravel	Gravelly Sand	Sandy Gravel	Sandy Gravel	Gravelly Sand	Sandy Gravel	Gravelly Sand	Gravel	Gravelly Sand	Sandy Gravel	Sandy Gravel	Gravelly Sand	Gravelly Sand	Gravelly Sand	Gravelly Sand	Sandy Gravel						
FOLK AND WARD METHOD (φ)	MEAN	-0.715	-2.072	-0.342	-0.756	-1.208	-0.991	-0.425	0.141	-0.444	-1.313	-0.196	-0.486	0.173	-2.741	-0.417	-1.487	-1.192	-0.348	0.015	0.782	-1.080	
	SORTING	2.330	1.878	2.237	1.761	2.044	2.042	1.855	1.895	1.371	1.672	1.663	1.179	1.631	0.668	1.037	1.895	1.507	1.231	0.883	1.280	1.995	
	SKEWNESS	0.233	0.828	-0.120	0.168	0.288	0.094	-0.022	-0.328	0.058	0.142	0.046	-0.170	0.050	0.221	-0.111	-0.008	0.061	-0.138	-0.218	-0.032	0.053	
	KURTOSIS	0.792	0.973	0.783	1.161	0.693	0.711	0.941	0.946	1.233	0.912	1.467	1.071	1.112	0.907	1.021	0.862	0.916	0.933	1.216	1.097	0.937	
FOLK AND WARD METHOD (Description)	MEAN :	Very Coarse Sand	Fine Gravel	Very Coarse Sand	Very Coarse Sand	Very Fine Gravel	Very Coarse Sand	Very Coarse Sand	Coarse Sand	Very Coarse Sand	Very Fine Gravel	Very Coarse Sand	Very Coarse Sand	Coarse Sand	Fine Gravel	Very Coarse Sand	Very Fine Gravel	Very Fine Gravel	Very Coarse Sand	Coarse Sand	Coarse Sand	Very Fine Gravel	
	SORTING:	VPS	PS	VPS	PS	VPS	VPS	PS	PS	PS	PS	PS	PS	PS	MWS	PS	PS	PS	PS	MS	PS	PS	
	SKEWNESS:	Fine Skewed	Very Fine Skewed	Coarse Skewed	Fine Skewed	Fine Skewed	Symmetrical	Symmetrical	Very Coarse Skewed	Symmetrical	Fine Skewed	Symmetrical	Coarse Skewed	Symmetrical	Fine Skewed	Coarse Skewed	Symmetrical	Symmetrical	Coarse Skewed	Coarse Skewed	Symmetrical	Symmetrical	
	KURTOSIS:	Platy	Meso	Platy	Lepto	Platy	Platy	Meso	Mesokurtic	Lepto	Meso	Lepto	Meso	Lepto	Meso	Meso	Platy	Meso	Meso	Lepto	Meso	Meso	

MEASKRON		MEA1-24/08	MEA2-24/08	MEA3-24/08-A	MEA3-24/08-D1	MEA3-24/08D
SIEVING ERROR:		0.3%	0.1%	2.2%	0.2%	0.1%
SAMPLE TYPE:		Uni, PS	Uni, MS	Uni, PS	Uni, MWS	Uni, MWS
TEXTURAL GROUP:		Sandy Gravel	Gravel	Sandy Gravel	Gravel	Gravel
FOLK AND WARD METHOD (φ)	MEAN	-1.490	-2.631	-1.336	-2.736	-3.292
	SORTING	1.259	0.899	1.077	0.608	0.548
	SKEWNESS	0.120	0.455	0.015	0.119	0.254
	KURTOSIS	1.018	0.968	1.037	0.997	0.787
FOLK AND WARD METHOD	MEAN :	Very Fine Gravel	Fine Gravel	Very Fine Gravel	Fine Gravel	Medium Gravel

WARD METHOD	SORTING:	PS	MS	PS	MWS	MWS
(Description)	SKEWNESS:	Fine Skewed	Very Fine Skewed	Symmetrical	Fine Skewed	Fine Skewed
	KURTOSIS:	Meso	Meso	Meso	Meso	Platy

MURGUESS		MURG-24/08-A	MURG-24/08-C	MURG-25/08-Ha	MURG-25/08-Hb	MURG-25/08-J	MURG-25/08-K	MURG-25/08-L	MURG-25/08-M1	MURG-25/08-M2	MURG-25/08-O1	MURG-25/08-O2	MURG-25/08-Q	MURG-25/08-R	MURG-25/08-S	MURG-25/08-T1	MURG-25/08-U	MURG-25/08-V	MURG-25/08-W	
SIEVING ERROR:		0.1%	0.1%	0.5%	0.3%	0.6%	-0.2%	0.2%	0.5%	0.3%	-0.4%	0.2%	0.1%	0.3%	0.1%	0.0%	0.2%	0.4%	0.2%	
SAMPLE TYPE:		Bi, PS	Uni, PS	Bi, PS	Tri, PS	Bi, PS	Bi, PS	Uni, PS	Uni, PS	Uni, PS	Bi, PS	Bi, PS	Bi, PS	Bi, PS	Bi, PS	Bi, PS	Bi, PS	Bi, PS	Bi, PS	
TEXTURAL GROUP:		Sandy Gravel	Sandy Gravel	Sandy Gravel	Sandy Gravel	Gravelly Sand	Sandy Gravel	Sandy Gravel	Gravelly Sand	Sandy Gravel										
FOLK AND WARD METHOD (φ)	MEAN	-1.300	-1.209	-1.212	-1.208	-0.158	-2.072	-0.992	-0.088	-0.920	-0.344	-1.173	-1.321	-0.781	-1.848	-1.384	-1.274	-0.607	-1.633	
	SORTING	1.343	1.055	1.676	1.867	1.561	1.483	1.549	1.387	1.114	1.698	1.190	1.357	1.845	1.409	1.176	1.201	1.440	1.747	
	SKEWNESS	-0.043	-0.012	-0.026	-0.009	-0.011	0.058	-0.136	0.199	0.023	-0.037	-0.021	-0.076	-0.187	-0.141	0.057	-0.105	0.070	-0.153	
	KURTOSIS	0.896	0.984	0.828	0.858	1.080	0.758	1.092	1.013	1.106	1.201	1.133	0.880	1.182	0.895	0.919	1.052	1.174	0.666	
FOLK AND WARD METHOD (Description)	MEAN :	Very Fine Gravel	Very Fine Gravel	Very Fine Gravel	Very Fine Gravel	Very Coarse Sand	Fine Gravel	Very Coarse Sand	Very Coarse Sand	Very Coarse Sand	Very Coarse Sand	Very Fine Gravel	Very Fine Gravel	Very Coarse Sand	Very Fine Gravel	Very Fine Gravel	Very Fine Gravel	Very Coarse Sand	Very Fine Gravel	
	SORTING:	PS	PS	PS	PS	PS	PS	PS	PS	PS	PS	PS	PS	PS	PS	PS	PS	PS	PS	PS
	SKEWNESS:	Symmetrical	Symmetrical	Symmetrical	Symmetrical	Symmetrical	Symmetrical	Coarse Skewed	Fine Skewed	Symmetrical	Symmetrical	Symmetrical	Symmetrical	Coarse Skewed	Coarse Skewed	Symmetrical	Coarse Skewed	Symmetrical	Coarse Skewed	
	KURTOSIS:	Platy	Meso	Platy	Platy	Meso	Platykurtic	Meso	Mesokurtic	Meso	Lepto	Lepto	Platy	Lepto	Platy	Meso	Meso	Lepto	Very Platy	

6.1 Measkron (MEA)

For all the analysed units of Measkron, the grain size distribution is unimodal (**Fig. 14b; table 4**). The deposits are much coarser than the ones of Humbepa and Murguess. The sorting (values of σ_ϕ , **table 4**) indicates well sorted to very well sorted units. The skewness is generally positive (fine skewed) and the kurtosis mesokurtic which reflects the low concentration around the mean, hence the low sorting of the layers. Even though σ_ϕ values indicate good sorting, other parameters indicate a lower degree of sorting.

The componentry analyses confirm that Measkron is invariably dominated by angular to rounded, red to brown juveniles that are poor in vesicles.

6.2 Murguess (MURG)

All sieving results show that the units are well sorted (**Cas and Wright, 1987; table 4**). However, the grain-size distribution is bimodal. As an exception, the thin bedded (TB) facies displays a kurtosis ranging from meso- to platykurtic, implying that the units are not that well sorted. The skewness is often symmetric which means that the grain size is evenly spread around the average. Several distributions are however negatively skewed implying a coarse skewness, i.e. the mean tends towards the larger grain size.

The thin beds follow mostly a unimodal distribution. The statistics obtained by GradiStat (**Blott and Pye, 2001**) display sometimes bimodal distribution, but the second mode is so minor that it can be considered unimodal.

The componentry analyses confirm that Murguess deposits are dominated by sub-spherical to ellipsoidal juvenile particles (loaded or cored), with abundant free phlogopite and few lithics.

6.3 Density Measurements

We compared texture variations (shape and composition) of clasts on their densities. For Murguess, clast density varies from 1.354 g/cm³ to 3.251 g/cm³ (average of 2.428 g/cm³) following an asymmetric almost normal distribution (skewness -0.67; kurtosis 0.33; **table 5**). We did not notice any density differences between loaded, cored, angular, or rounded juveniles. The densities obtained with the He-pycnometer can increase the whole-rock density values (obtained from the GeoPyc 1360 pycnometer) from 0 to maximum 38% (**table 6**).

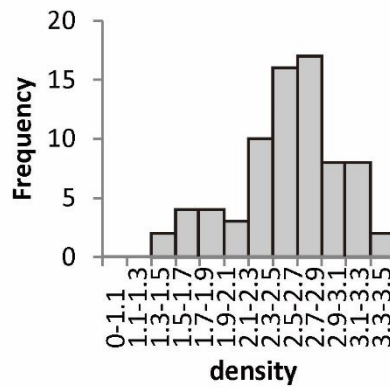
For Measkron, the density varies from 1.137 to 3.514 g/cm³ (average of 2.356 g/cm³) following a symmetrical leptokurtic distribution (skewness -0.02; kurtosis 0.52; **table 5**). We did not notice any

density differences between loaded, cored, angular, or rounded juveniles. The densities obtained with the He-pycnometer can increase the whole-rock density values from 0 to maximum 268% (table 6). Note that this high value is the extreme outlier and hence, not representative, the mean being 58% increase and the median 44%.

Table 5: whole rock density (in g/cm³) analyses measured with the GeoPyc 1360 pycnometer

Murguess

Mean	2.428
Standard Error	0.048
Median	2.448
Mode	#N/A
Standard Deviation	0.409
Sample Variance	0.167
Kurtosis	0.333
Skewness	-0.667
Range	1.897
Minimum	1.354
Maximum	3.251
Sum	179.688
Count	74



Measkron

Mean	2.356
Standard Error	0.047
Median	2.347
Mode	2.544
Standard Deviation	0.413
Sample Variance	0.170
Kurtosis	0.527
Skewness	-0.020
Range	2.377
Minimum	1.137
Maximum	3.514
Sum	183.794
Count	78

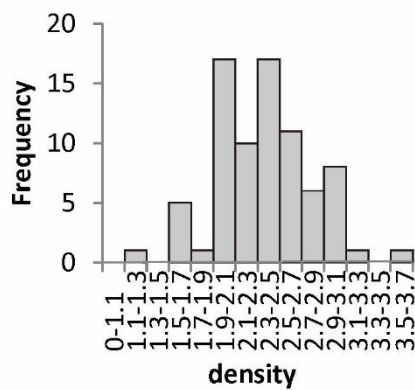


Table 6: whole rock density (in g/cm³) analyses measured with the He-pycnometer, compared with the values obtained with the GeoPyc 1360 pycnometer. The difference gives an estimation of microporosity.

MURGUESS				MEASKRON			
GeoPyc	He Pycno	Δ	%increase	GeoPyc	He Pycno	Δ	%increase
2.389	2.948	0.560	23	2.587	3.174	0.587	23
2.556	2.833	0.277	11	2.900	3.540	0.640	22
2.992	3.048	0.055	2	2.218	4.082	1.863	84
2.131	2.948	0.817	38	1.997	3.369	1.372	69
2.235	2.911	0.676	30	2.729	3.368	0.639	23
2.620	2.621	0.000	0	2.076	5.176	3.100	149
2.445	2.877	0.432	18	2.444	4.368	1.925	79
2.549	2.873	0.324	13	2.916	3.995	1.080	37
2.288	2.923	0.635	28	3.137	4.860	1.723	55
2.330	2.858	0.528	23	1.137	4.188	3.051	268
2.374	2.776	0.402	17	2.306	3.719	1.413	61
2.595	2.883	0.288	11	2.557	4.325	1.768	69
2.755	2.815	0.060	2	2.096	4.569	2.472	118
2.849	3.029	0.180	6	2.315	5.075	2.760	119
2.641	2.779	0.137	5	2.846	2.725	-0.122	-4
2.423	2.780	0.357	15	2.517	3.047	0.531	21
				2.492	3.068	0.575	23
				3.055	3.258	0.203	7
				2.080	3.153	1.073	52
				2.544	2.783	0.239	9
				2.099	3.067	0.968	46
				2.148	3.098	0.950	44
				2.379	3.181	0.802	34
				1.789	3.197	1.408	79
				2.304	3.019	0.715	31
				2.506	3.062	0.556	22
				2.536	3.088	0.552	22

7. DISCUSSION

7.1 Eruption dynamics

Our study highlights various type of deposits which might reflect various eruptive style and conditions.

Bambahay

The basal units J-I-H of Bambahay suggests an initial emplacement resulting from phreatomagmatic activity, with the presence of accretionary lapilli and abundance of fine yellow ash, the colour being

probably due to palagonatization. This activity was dominated by dilute pyroclastic density currents that deposited ash packages up to ~3,5 m. The units F and G correspond to multiple pyroclastic density currents, and, considering the size of the beds, of small volume. At the late stage, a short phase of Strombolian activity deposited the thin layer of scoria fall (SIN-E). Then, the phreatomagmatic activity resumed with emplacement of pyroclastic density currents (units A and C). We hence suggest that water availability was fluctuating during the eruption, and units D and B might correspond to adjustments and dynamic transition.

Humbepa and Nangwa

At Humbepa, the facies α (massive ash beds) might correspond to periods of sustained pyroclasts emission that allowed the emplacement of single-size particles with limited crater excavation (few larger lithics). Ticker bed might reflect a long eruptive phase or a more important flow rate. Facies α corresponds to the emplacement from dilute pyroclastic density currents, as attested by non-constant bed thickness and trachytic texture. Facies β with its diffusely to very diffusely stratified mm-thin beds, with cross-bedding and non-constant bed thickness, suggest discrete pyroclastic density currents of small volume. Because there is no continuity of the units across the ~200 m long outcrop and the facies β is observed at multiple places (ie. no specific pattern in facies distribution), we conclude that these pulses occurred in several directions.

The variety of facies at Humbepa reveal complex eruption dynamics, reflecting changing eruptive conditions.

The pluridirectional and multiple small events might, perhaps, reflect different loci and/or timing of explosion within the crater. The facies γ with its massive and strongly unsorted thick beds might correspond to local collapse of deposits that slide back into the crater, or phases of tephra jets that clear off the crater filled with debris and forming ballistic curtains ([Valentine et al., 2017](#)). The three facies highlight dynamic and changing eruptive conditions that produced the Humbepa deposits. Nangwa might have originated from similar eruption dynamics as Humbepa with its facies α (Nangwa) reflecting multiple pulses, which produced pyroclastic density currents. These explosive episodes were separated by either periods of pause, followed by tephra jets, or by crater enlargement (facies β of Nangwa).

Murguess

The deposit sequence of Murguess is less diverse than that of Humbepa in terms of componentry and eruptive style. The deposits are dominated by spherical and ellipsoidal juvenile particles. The presence of lenses, low-angle cross-bedding, inverse grading, and poorly-sorted layers points towards material mainly deposited from pyroclastic density currents. It is possible that some of the

material was deposited through fall, considering the lack of fine ash. We only sampled proximal deposit and fine ash might lay further away. Ngarenalo deposits are similar than those of Murguess in terms of cannon-ball bomb and sub-spherical juvenile abundance, but the laminated beds are similar to the facies β of Humbepa. This deposit implies an efficient fragmentation from an explosive eruptive column in combination with more Strombolian-like jetting.

Measkron

Measkron deposits shows emplacement characteristics of both pyroclastic density current and tephra fall. Some units of the deposit are clast-supported and show little variation in grain-size compared to what we can expect for pyroclastic density currents (MEA1 and 2). The particles are welded together but do not show fiamme morphology. The crude bedding and the crude cross-bedding at MEA2 might thus correspond to several fall episodes accompanied by grain avalanching, due to the steepness of the cone. Note that it is difficult to assess the continuity of bed thickness with the limited availability of outcrops. The thin ash beds and lenses at MEA 3 are likely related to dilute and non-dilute pyroclastic density currents, with thin beds of variable thickness and cross-bedding that form lenses.

Based on our field observations, we suggest a decrease of water influence from Bambahay type, to Humbepa type, to Murguess type and to Measkron type. A previous study in the Natron area, further north of our field study, further suggested that water was not needed to form the maar field and instead rapid decompression of gas-rich magmas may have been responsible for maar formation ([Berghuijs and Mattsson, 2013](#)). [White and Valentine \(2016\)](#) warned, however, for the use of lack of clear depositional and textural indicators of phreatomagmatism as evidence for magmatic fragmentation. In the rest of the discussion, we will hence present several aspects and discuss them with an emphasis on evidence for “dry” or “wet” fragmentation.

7.2. Xenoliths and bombs

It is commonly accepted that eruptions or eruptive phases that involve water produce lithic-rich deposits ([Lorenz, 1986](#); [Houghton et al., 1996](#); [White and Ross, 2011](#) and reference therein). Tuff rings and tuff cones have generally lower proportions of lithics ([Lorenz, 1986](#)).

Lithic-rich units were found in Humbepa crater and Bambahay, but in general the deposits are not rich in lithics. Most of the craters in the studied zone are shallow tuff rings rather than deep maars. Water infill and hence lacustrine sedimentation is limited in this area, but it is possible that the real depth of craters is partly concealed due to erosion-related infill. However, the limited water

availability, the relatively young age (Pleistocene), might point towards a limited secondary infill. The shallow depth of the craters might explain the low proportions of lithics in the deposits, except if we consider that multiple blasts have hidden the initial deep crater ([Macorps et al., 2016](#)).

Interestingly, large juvenile bombs (>10 cm) were not observed in any of the tephra deposits, while large lithic blocks (up to 20 cm in size) were encountered. Only one large granite-like block of about 70 cm across has been observed at the base of the Humbepa deposits.

The amount of lithics in Humbepa and Bambahay might point towards wetter eruptions compared to the rest of the craters. Possibly, the lack of larger lithics and bombs (bigger than 20cm across) might reflect low-energy explosions, as previously suggested by the low depth of the crater.

7.3. Grain size

Phreatomagmatic eruptions are generally known to produce finer grained deposits, although coarser grain sizes can be produced ([Fisher and Schmincke, 1984](#)). Similarly, grain-size analyses might be biased by the sampling method. All those critiques can be found in the paper of [White and Valentine \(2016\)](#).

As briefly discussed earlier, our sieving analyses results of Humbepa and Measkron are biased by particle clustering. We could not determine for Humbepa if this clustering is primary and resulting from syn-eruptive agglutination in the crater, or due to secondary cementation. Even considering the cautions formulated by [White and Valentine \(2016\)](#), we can observe with the grain size analysis and with naked eyes enrichment in finer-grained clasts at Humbepa compared to Measkron and Murguess. The finer grain size in Humbepa might point towards wetter eruptions compared to the other studied volcanoes. This also fits with the deeper crater and the higher content of lithics in Humbepa.

7.4. Pyroclastic density currents

Phreatomagmatic eruptions produce dilute pyroclastic density currents (PDCs) or base surges ([Cas and Wright, 1987](#)). The resulting deposits are stratified, laminated or massive, with juvenile, lithics and free crystals. The deposit can be e.g. planar-bedded, can form U-shape erosional channels, dunes, chutes and pools etc, depending on the flow's turbulence. The deposits generally show evidence for being wet, with for example plastic deformation with impact sags below large bombs, accretionary lapilli, plastering against steep surface, etc.

Some layers of the Bambahay deposit show clear evidence for a base surge origin with erosional channels, wavy beds, and accretionary lapilli. At Humbepa, the layers of unit HUM12 C and D are crudely bedded, unsorted, with lithics and accretionary lapilli. One of the large lithics seems to have

deformed the layer below plastically. These units have been likely deposited through dilute pyroclastic density currents. We also suggest that the facies α of Humbepa to have been deposited through this mechanism.

As discussed earlier, we infer that most of the deposits of the maar and tuff rings have been deposited through pyroclastic density currents. Evidence of wetness is absent at Murguess and Measkron, and to some extent at Ngarenalo, pointing towards less humid conditions. Antidunes are marker of high energy flow. Since they are present but not abundant, we suggest that most of the PDCs emplaced with rather low energy. Inverse grading in Murguess points most likely towards dry deposit where particles are able to roll back through grain avalanching. Furthermore, grain avalanching was possibly facilitated by the ellipsoidal shape of the pyroclasts.

7.5. Particle shape: spherical and ellipsoidal lapilli and cannonball bombs

Because of the high energy released during magma-water interaction, the particles are expected to be angular and quenched, but it has been shown via experiments and field observations that a large spectrum of particle shapes can be produced by magma/water interaction ([Zimanowski et al., 1997](#)). This is partially explained by the fact that not all the magma will interact with water and by recycling processes in the vent ([Büttner et al., 2002](#); [Rosseel et al., 2006](#)).

In our field area, several deposits are dominated by rounded juvenile particles, which is still surprising if only phreatomagmatism was involved. As mentioned earlier, the deposits are not bomb-rich and the grain size for the juveniles range from ash to coarse lapilli. The pyroclast shapes range from spherical to ellipsoidal but are more prolate than oblate in shape.

The thin ash coating around lapilli observed in Humbepa and Ngarenalo deposits is similar to the descriptions of [Houghton and Schmincke \(1989\)](#) and [Houghton and Smith \(1993\)](#). These authors suggested that the coating is made of wet ash that adheres and is baked by the clasts which were still hot. Hence, ash coating around lapilli indicates phreatomagmatic or wet (rain) conditions. Ash coating could explain the cementation of Humbepa and some Ngarenalo units, where the thin film of humidified ash around the clasts cement them together once the ash dries out.

The rounded and loaded lapilli are similar to loaded bombs (in composition) and cannon-ball bombs (in morphology) ([Francis, 1973](#); [Rosseel et al., 2006](#)). Subspherical shapes of lapilli and bombs have been observed at scoria cones and tuff rings/maars across the world ([Francis, 1973](#); [Alvarado et al., 2011](#); [Delpit et al., 2014](#)). The shape has been attributed to surface tension ([Lorenz and](#)

Zimanowski, 1984), to rolling along the flank or the deposit (Francis, 1973; Murcia et al., 2015), to recycling processes (Alvarado et al., 2011), or to magma viscosity (Comida et al., 2017). Their presence in a maar deposit is thought to be an evidence of a drying up of the system, or unequal distribution of water (Murcia et al., 2015). The composition of the subspherical loaded bombs and lapilli is reflecting recycling within the vent (“loaded” bomb, Rossel et al., 2006).

Most of the subspherical bombs and lapilli have been observed in intra-plate tectonic settings and associated with low viscosity and high temperature magmas (Alvarado et al., 2011). They have been also observed in Herchenberg volcano in Germany, with similar ultra-alkaline composition than the one of our studied area (Bednarz and Schmincke, 1990). These authors inferred that the eruption started with a phreatomagmatic phase that evolved into a Strombolian eruption. They noticed an abundance of subspherical lapilli within the Strombolian deposit. Even though a formation mechanism for such shape was not proposed, the characteristics of the deposits were attributed to eruptions of typically high proportions of magmatic gas (mainly CO₂) relative to low viscosity magma. In other words, variable chemical compositions, volatile contents, and related physical properties of magmas are important parameters to control the eruptive style. In the same line with e.g. Francis (1973), Bednarz and Schmincke (1990) proposed that the inversely graded layers resulting from grain avalanching were further facilitated by the ellipsoidal, smooth shaped of the lapilli. However, because they found reverse grading near the crater wall, they suggest that this process might not only be due to sorting but must reflect changes in eruptive dynamics. Such subspherical juvenile lapilli have also been observed in ultramafic diatremes (Delpit et al., 2014). Preliminary results of experimental modelling tend to show that the shape is related to the viscosity rather than to eruptive conditions (wet or dry) (Comida et al., 2017). Subspherical morphology might hence not be related to the interaction with water and magma but related to the magma composition and gas content. The fluidal texture found in several cored and loaded ash and lapilli with microcrystals surrounding the largest phenocrysts also suggests low viscosity magma.

7.6. Vesicles

Phreatomagmatic deposits generally present a complete spectrum of vesicularity from dense non-vesicular particles to highly vesicular ones, depending on the depth level at which water encounters the magma (Houghton and Schmincke, 1989). The studied deposits display such diversity in porosity and most of the particles have no vesicles or present a microvesicularity as observed through binocular or with the He-pycnometer data. For Measkron, the large density range is likely due to a welding effect, where pyroclasts agglutinate together and become denser with the pressure of the deposit pile above or can be due to secondary infill of vesicles. The microvesicularity suggests that fragmentation has happened before complete vesiculation, hence there was no time to

expand the gas and create larger vesicle before fragmentation. Yet, another possibility to explain this microvesicularity is that the gas phase has already escaped and has been decoupled from the magma. Recycling processes within the conduit might also lead to dense non-vesicular particles (Guilbaud et al., 2009).

7.7. Proposed model

The deposits share similarities with kimberlite maar-diatremes, mainly in the abundance of spherical and ellipsoidal lapilli (Mitchell, 1986; Kurszlaukis et al., 1998; Llyod and Stoppa, 2003; Porritt and Cas, 2009). Such lapilli can be made of a kernel surrounded by kimberlite (pelletal lapilli) or without any kernel (composite lapilli). One of the debates animating the kimberlite maar-diatreme community is the wet or dry fragmentation at the origin of the eruption (Kurszlaukis et al., 1998; Sparks et al., 2006; Stoppa et al., 2013). The common observation is that ultra-mafic and alkaline rich magma behave in a different way, and it is common to observe sub-spherical lapilli and bombs in deposits with this composition (Llyod and Stoppa, 2003; Comida et al., 2017).

From our field survey, it is not clear yet how much the gas or the water influenced the fragmentation and we observe deposits that indicate moderately wet conditions to less wet conditions.

Spatial distribution analysis of volcanic alignments in Manyara shows an initial dominant control of regional rift structures and old basement on the distribution of volcanic vents (Delcamp et al., 2019). It is suggested that the influence of the tectonic structures is fading, and that the rift is entering a more mature phase. Alternatively, the numerous volcanic alignments could reflect high magma pressure (see Discussion in Delcamp et al., 2019; Jolly and Sanderson, 1997).

We hence propose that the faults allow the gas-rich alkaline low viscosity magma to rise quickly giving less time for the gas to decouple from the magma. The gas decouples only near the surface resulting in a two-phase jet with a gas phase and a partially degassed magma phase. If the magma does not meet water or only very limited amounts, a dry eruption will occur (e.g. Murguess). If a fracture hosts a small aquifer, a phreatomagmatic eruption will occur (e.g. Humbepa). Nevertheless, signs of water-magma interaction will be limited in phreatomagmatic deposits because of the limited water amount available within a fracture (compared to e.g. a lake or a river) and keeping in mind that not all the magma will interact with the water. Indeed, only parts of the melt and the water are involved during the process of heat transfer and fragmentation (Molten Fuel-Coolant Interaction; MFCI; Zimanowski et al., 2015). The microvesicularity indicates that interaction with water occurred quickly after vesiculation initiation. In our model, fast rising magma would allow to maintain physical conditions similar throughout the path, and the level of interaction (deep or shallow) will not have major consequences on the final deposit texture. Once at the surface, the

magma is degassed and can form a lava pool at the dyke tip, similar to the one formed at Ukinrek maar, Alaska (Kienle et al., 1980).

Sub-spherical juvenile particles could be formed by both surface tension and bubble outburst when new magma arrives, by recycling processes within a lava pool (if present), by fluidization (by juvenile gas) of the magma within the conduit (Stoppa et al., 2003), due to low viscosity (Comida et al., 2017), or immiscibility. Furthermore, the spherical and ellipsoidal shape of the particles suggests ductile fragmentation which occurred in a liquid state rather than in a solid state as it could occur during magma-water interaction. Because of low viscosity, the gas should escape easily, but the faults and the low viscosity of the magma in a confined space allows the magma to rise fast. Interaction with water will trigger more violent eruptions and will form deeper maars with finer grained deposits. Such violent eruptions with alkaline mafic magma have been reported in Goma, DRC (Poppe et al., 2016). Drier fragmentation will form shallow craters with tuff rings or tuff cones with larger particles. However, the general shallow depth of the craters in the field area (Delcamp et al., 2019) and the lack of large bombs suggests that explosions were only mildly violent, which fits with a partially degassed magma and limited contact with water. Such model could explain the lack of classical “water-magma” interaction evidence across the field and the diversity of deposits from relatively classical maar evolution with a shift between drier (Strombolian) phases and phreatomagmatic activity (Bambahay), to relatively wet deposits with a maar crater (Humbepa), to intermediate deposits (Ngarenalo) and dry ones (Murguess, Measkron).

With this paper, we propose a conceptual model, and our field study is a first step. We hope to trigger discussions and to drag the community towards the uncommon character of the poorly studied volcanoes of Tanzania, and similar deposit elsewhere. This model needs further constrains with more textural analyses of sub-spherical lapilli, and a study of mineral inclusion for volatile content to estimate volatile budget and degassing would be highly valuable.

CONCLUSION

Field observations, crater morphology, grain size analyses, and componentry highlight a large variation of eruptive styles within the volcanic fields of Hanang and Babati, Tanzania. We suggest that this variation is linked to an interplay between the dissolved gas content in the ascending magma and the amount of water available for fragmentation. As a result, the inferred eruptive intensity in the area has ranged from violent fragmentation with water involvement and maar formation to less violent fragmentation with tuff ring and tuff cone formation, linked to gas expansion within a mafic alkaline gas-rich magma (dry fragmentation). Further investigations are needed to understand the complex mechanism of vesiculation and fragmentation in monogenetic

volcanoes of North Tanzania and in general for alkaline magma.

ACKNOWLEDGEMENTS: We would like to acknowledge Maliki Maliki and Ceven Shemsanga for assistance in the field and Karen Fontijn, Sam Poppe, Pierre-Simon Ross and Pier Paolo Comida for discussion. Sam, thank you for helping me with the last draft and motivating me to end up this nightmare by uploading it on EarthArxiv. The research has been funded by FWO-Vlaanderen and access to the field has been possible thanks to the Tanzanian Commission for Science and Technology (COSTECH). We would like to thank Lydia Zehnder for chemical analysis at ETH Zürich and Jean Marc Hénot for use of SEM at LMV, Clermont-Ferrand.

CONTRIBUTION:

Audray Delcamp: main researcher

Lucia Gurioli: textural analyses and discussion

Hannes Mattson: chemical analyses and discussion

Engelbert Sakoma: field assistant

Lore Steyaert: grain size analyses

Matthieu Kervyn: discussion

References:

Alvarado, G.E., Soto, G.J., Salani, F.M., Ruiz, P., Hurtado de Mendoza, L. (2011). The formation and evolution of Hule and Río Cuarto maars, Costa Rica. *J. Volcanol. Geotherm. Res.*, 201, 342–356

Bagdasaryan, G.P., Gerasimovskiy, V.I., Polyakov, A.I., Gukasyan, R.K. (1973). Age of volcanic rocks in the rift zones of East Africa. *Geochemistry International* 10, 66–71.

Baudouin, C., Parat, F., Denis, C.M.M., Mangasini, F. (2016). Nephelinite lavas at early stage of rift initiation (Hanang volcano, North Tanzanian Divergence). *Contrib. Mineral. Petrol.* 171: 64.

Berghuijs, J.F., Mattsson, H.B. (2013). Magma ascent, fragmentation and depositional characteristics of “dry” maar volcanoes: Similarities with vent-facies kimberlite deposits. *J. Volcanol. Geotherm. Res.*, 252, 53-72.

Bednarz, U., Schmincke, HU. (1990). Evolution of the quaternary melitite-nephelinite Herchenberg volcano (East Eifel). *Bull. Volcanol.* 52, 426.

Blott, S.J., Pye, K. (2001). GRADISTAT: a grain size distribution and statistics package for the analysis of unconsolidated sediments. *Earth Surf. Proces. Landforms* 26, 1237-1248.

Bradshaw, T.K., Smith, E.I. (1994). Polygenetic Quaternary volcanism at Crater Flat, Nevada. *J. Volcanol. Geotherm. Res.* 63, 165–182.

Büttner, R., Zimanowski, B. (1998). Physics of thermohydraulic explosions. *Phys. Rev. E*

57, 5726e5729.

Büttner, R., Dellino, P., La Volpe, L., Lorenz, V., Zimanowski, B. (2002). Thermohydraulic explosions in phreatomagmatic eruptions as evidenced by the comparison between pyroclasts and products from Molten Fuel Coolant Interaction experiments. *J. Geophys. Res.*, 107, B11, doi:10.1029/2001JB000511.

Brooker, R.A., Kohn, S.C., Holloway, J.R., McMillan, P.F. (2001). Structural controls on the solubility of CO₂ in silicate melts. Part I: bulk solubility data. *Chemical Geology* 174, 225–239.

Cas, R.A.F., Wright, J.V. (1987). *Volcanic Successions Modern and Ancient*. Unwin Hyman, Boston <http://dx.doi.org/10.1007/978-94-009-3167-1> (528 pp.)

Chorowicz, J. (2005). The East African rift system. *Journal of African Earth Sciences* 43, 379-410, doi: 10.1016/j.jafrearsci.2005.07.019.

Dawson, J.B. (2008). The Gregory Rift Valley and Neogene– Recent Volcanoes of Northern Tanzania. *Geological Society of London Memoir* 33, 102 p.

Deer, W.A., Howie, R.A., Zussman, J. (1962). *Rock-forming minerals*. Sheet Silicates, vol. 3. Longman, London, p. 270.

Delpit, S., Ross, P.-S., and Hearn, B.C. (2014). Deep-bedded ultramafic diatremes in the Missouri River Breaks volcanic field, Montana, USA: 1 km of syn-eruptive subsidence. *Bull. Volcanol.* 76, 7, 1–22

Delcamp A., Mossoux S., Belkus H., Tweheyo, C., Mattsson H.B., Kervyn M. (2019). Control of the stress field and rift structures on the distribution and morphology of explosive volcanic craters in the Manyara and Albertine rifts. *Journal of African Earth Sciences* 150: 566-583.

Delvaux, D., Barth, A. (2010) African Stress Pattern from formal inversion of focal mechanism data, implications for rifting dynamics. *Tectonophysics* 482,105-128.

de Silva, S., Lindsay, J.M. (2015). Primary Volcanic Landforms, in: Sigurdsson, H., Houghton, B., McNutt, S., Rymer, H., Stix, J. (2nd Ed), *The Encyclopedia of Volcanoes*. Academic Press, pp. 273-297.

Ebinger, C., Poudjom Djomani, Y., Mbede, E., Foster, A., Dawson, J.B. (1997). Rifting Archaean lithosphere: the Eyasi-Manyara-Natron rifts, East Africa. *Journal of the Geological Society*, London, 154, 947–960.

Eychenne, J., Le Penneç, J.L. (2012). Sigmoidal particle density distribution in a subplinian scoria fall deposit. *Bull. Volcanol.* 74: 2243

Fisher, R.V., Schmincke, H.-U. (1984). *Pyroclastic Rocks*: Berlin, Springer-Verlag, 472 p.,

doi: 10.1007/978-3-642-74864-6.

Francis, P.W. (1973). Cannonball bombs, a new kind of volcanic bomb from the Pacaya Volcano, Guatemala. *Geol. Soc. Amer. Bull.* 84, 2791–2794

Freda, C., Gaeta, M., Karner, D., Marra, F., Renne, P., Taddeucci, J., Scarlato, P., Christensen, J., Dallai, L. (2006). Eruptive history and petrologic evolution of the Albano multiple maar (Alban Hills, Central Italy). *Bull. Volcanol.* 68, 567–591.

Graettinger, A.H., Valentine, G.A., Sonder, I., Ross, P.-S., White, J.D.L., and Taddeucci, J. (2014). Maar-diatreme geometry and deposits: Subsurface blast experiments with variable explosion depth. *G³*, 15, 740–764, doi:10.1002/2013GC005198.

Guilbaud, M.-N., Siebe, C., Agustín-Flores, J. (2009). Eruptive style of the young high-Mg basaltic-andesite Pelagatos scoria cone, southeast of México City. *Bull. Volcanol.* 71 (8), 859–880

Harvey, S., Kjarsgaard, B., McClintock, M., Shimell, M., Fourie, L., Plessis, P.D., Read, G. (2009). Geology and evaluation strategy of the Star and Orion South kimberlites, Fort à la Corne, Canada. *Lithos.* 112 (S1), 47–60.

Head, J.W., Sparks, R.S., Bryan, W.B., Walker, G.P.L., Greely, R., Whitford-Stark, J.L., Guest, J.E., Wood, C.A., Shultz, P.H., Carr, M.H. (1981). Distribution and morphology of basalt deposits on planets. *Basaltic Volcanism on the Terrestrial Planets*. Pergamon Press Inc, New York, pp. 701–800.

Houghton, B.F., Schmincke, H.-U. (1989). Rotenberg scoria cone, East Eifel: a complex Strombolian and phreatomagmatic volcano. *Bull. Volcanol.* 52, 28–48.

Houghton, B.F., Smith, R.T. (1993). Recycling of magmatic clasts during explosive eruptions: estimating the true juvenile content of phreatomagmatic volcanic deposits. *Bull. Volcanol.* 55, 414–420.

Houghton, B.F., Wilson, C.J.N., Rosenberg, M.D., Smith, I.E.M., Parker, R.J. (1996). Mixed deposits of complex magmatic and phreatomagmatic volcanism: An example from Crater Hill, Auckland, New Zealand. *Bull. Volcanol.* 58, 59–66, doi:10.1007/s004450050126.

Jarvis, A., Reuter, H.I., Nelson, A., Guevara, E. (2008). Hole-filled SRTM for the globe 706 Version 4, available from the CGIAR-CSI SRTM 90m Database 707 (<http://srtm.csi.cgiar.org>).

Jolly, R.J.H., Sanderson, D.J. (1997). A Mohr circle construction for the opening of a pre-existing fracture. *J. Structural Geol.* 19 (6), 887–892.

Kienle, J., Kyle, P.R., Self, S., Motyka, R.J., Lorenz, V. (1980). Ukinrek Maars, Alaska, I. April 1977 eruption sequency, petrology and tectonic setting. *J. Volcanol. Geotherm. Res.* 7, 11-37.

Kurszlaukis, S., Büttner, R., Zimanowski, B., Lorenz, V. (1998). On the first experimental phreatomagmatic explosion of a kimberlite melt. *J. Volcanol. Geotherm. Res.* 80, 323–326.

Lorenz, V. (1973). On the formation of maars. *Bull. Volcanol.* 37, 183–204.

Lorenz, V. (1986). On the growth of maars and diatremes and its relevance to the formation of tuff rings. *Bull. Volcanol.* 48, 265–274.

Lorenz, V. (2003). Maar-Diatreme Volcanoes, their Formation, and their Setting in Hard-rock or Soft-rock Environments. *Geolines* 12, 72-83.

Lorenz, V., Zimanowski, B. (1984). Fragmentation of alkali basaltic magmas and wall-rocks by explosive volcanism, in IIIème Conference International Kimberlites, edited by J. Kornprobst, pp. 73 – 83, Univ. de Clermont-Ferrand, Clermont, France.

Lloyd, F.E., Huntingdon, A.T., Davies, G.R., Nixon, P.H. (1991). Phanerozoic volcanism of southwest Uganda: a case for regional K and LILE enrichment of the lithosphere beneath a domed and rifted continental plate. In: *Magmatism in Extensional Structural Settings. The Phanerozoic African Plate.* Edited by Kampunzu, A. B. and Lubala, R. T.) p 23-72. Springer-Verlag, Heidelberg.

Macheyeki, A.S., Delvaux, D., De Batist, M., Mruma, A. (2008). Fault kinematics and tectonic stress in the seismically active Manyara–Dodoma Rift segment in Central Tanzania – Implications for the East African Rift. *J. of African Earth Sci.* 51, 163–188.

Macorps, E., Graettinger, A.H., Valentine, G.A., Ross P-S, White, J.D.L., Sonder, I. (2016). The effects of host-substrate properties on maar-diatreme volcanoes: experimental evidence. *Bull. Volcanol.* 78, 26, doi:10.1007/s00445-016-1013-8

Mitchell, R.H. (1986). Kimberlites: Mineralogy, Geochemistry and Petrology. *Plenum Press*, NY, p. 442.

Mudd, G.C., Orridge, G.R. (1966). Quarter Degree Sheet 85: Babati, Mineral Resources Division, Tanzania, scale 1:125,000.

Murcia, H., Németh, K., El-Masry, N.N., Lindsay, J.M., Moufti, M.R.H., Wameyo, P., Cronin, S.J., Smith, I.E.M., Kereszturi, G. (2015). The Al-Du'aythah volcanic cones, Al-Madinah City: implications for volcanic hazards in northern Harrat Rahat, Kingdom of Saudi Arabia. *Bull. Volcanol.* 77 (6), 1–19.

Poppe, S., Smets, B., Fontijn, K. et al., (2016). Holocene phreatomagmatic eruptions alongside the densely populated northern shoreline of Lake Kivu, East African Rift: timing and hazard implications. *Bull. Volcanol.* 78: 82. <https://doi.org/10.1007/s00445-016-1074-8>

Porritt, L.A., Cas, R.A.F. (2009). Reconstruction of a kimberlite eruption, using an integrated volcanological, geochemical and numerical approach: a case study of the Fox Kimberlite, NWT, Canada. *J. Volcanol. Geotherm. Res.*, 179, 241–264.

Riedel, C., Ernst, G., Riley, M. (2003). Controls on the growth and geometry of pyroclastic constructs. *J. Volcanol. Geotherm. Res.* 127, 121–152.

Rosseel, J.-B., White, J. D. L., Houghton B. F. (2006). Complex bombs of phreatomagmatic eruptions: Role of agglomeration and welding in vents of the 1886 Rotomahana eruption, Tarawera,

New Zealand. *J. Geophys. Res.*, 111, B12205, doi:10.1029/2005JB004073.

Scott-Smith, B.H. (2008). Canadian kimberlites: geological characteristics relevant to emplacement. *J. Volcanol. Geotherm. Res.* 174(1–3), 9–19

Sparks, R.S.J., Baker, L., Brown, R.J., Field, M., Schumacher, J., Stripp, G., Walters, A. (2006). Dynamical constraints on kimberlite volcanism. *J. Volcanol. Geotherm. Res.* 155, 18–48

Stoppa, F. (1996). The San Venanzo maar and tuff ring, Umbria, Italy: eruptive behaviour of a carbonatite-melilitite volcano. *Bull. Volcanol.* 57, 563–577.

Stoppa, F., Schiazza, M. (2013). An overview of monogenetic carbonatitic magmatism from Uganda, Italy, China and Spain: Volcanologic and geochemical features. *J. South Am. Earth Sciences* 41, 140–159.

Sohn, Y. K. (1996). Hydrovolcanic processes forming basaltic tuff rings and cones on Cheju Island, Korea. *Geol. Soc. Amer. Bull.* 108(10), 1199–1211.

Thomas, C.M., James, T.C., Downie, C., Wilkinson, P. (1966). Quarter Degree Sheets 84, Hanang: Dodoma, Tanzania Mineral Resources Division, scale 1:125,000.

Valentine, G.A., Graettinger, A.H., Macorps, E., Ross, P.-S., White, J.D.L., Döhring, E., and Sonder, I. (2015). Experiments with vertically- and laterally-migrating subsurface explosions with applications to the geology of phreatomagmatic and hydrothermal explosion craters and diatremes. *Bull. Volcanol.* 77, 15, doi:10.1007/s00445-015-0901-7.

Valentine, G.A., White, J.D.L., Ross, P.-S., Graettinger, A.H., Sonder, I. (2017). Updates to concepts on phreatomagmatic maar-diatremes and their pyroclastic deposits. *Frontiers in Earth Science* 5:68, doi:10.2289/feart.2017.00068

Vespermann, D., Schminke, H.-U. (2000). Scoria cones and tuff rings. In: Sigurdsson, H., Houghton, B.F., McNutt, S.R., Rymer, H., Stix, J. (Eds.), *Encyclopedia of Volcanoes*. Academic Press, San Diego, 683–694.

White, J.D.L., Ross, P.-S. (2011). Maar-diatreme volcanoes: A review. *J. Volcanol. Geotherm. Res.* 201, 1–29.

White, J.D.L., Valentine, G.A. (2016). Magmatic versus phreatomagmatic fragmentation: Absence of evidence is not evidence of absence. *Geosphere* 12, 5: 1–11, doi: 10.1130/GES01337.1.

Wohletz, K.H. and Sheridan, M.F. (1983). Hydrovolcanic explosions II. Evolution of basaltic tuff rings and tuff cones. *American J. of Science*, 283(5): 385–413.

Zimanowski, B., Büttner, R., Dellino P., White J.D.L, Wohletz, K.H (2015). Magma–Water Interaction and Phreatomagmatic Fragmentation. In : Sigurdsson, H. (Ed.), *The Encyclopedia of Volcanoes (Second Edition)*. Academic Press, 473–484.

Zimanowski, B., Büttner, R., Lorenz, V. (1997). Premixing of magma and water in MFCI experiments. *Bull. Volcanol.* 58, 491–495, doi:10.1007/s004450050157.

